



WiNDS: An H_{α} Kinematics Survey of Nearby Spiral Galaxies—Vertical Perturbations in Nearby Disk-type Galaxies

Catalina Urrejola-Mora¹ , Facundo A. Gómez^{1,2} , Sergio Torres-Flores¹, Philippe Amram³, Benoît Epinat^{3,4}, Antonela Monachesi^{1,2} , Federico Marinacci⁵ , and Claudia Mendes de Oliveira⁶

¹ Departamento de Astronomía, Universidad de La Serena, Av. Juan Cisternas 1200 Norte, La Serena, Chile; catalina.m.urrejola@gmail.com

² Instituto de Investigación Multidisciplinar en Ciencia y Tecnología, Universidad de La Serena, Raúl Bitrán 1305, La Serena, Chile

³ Aix Marseille Univ. University, CNRS, CNES, LAM, Marseille, France

⁴ Canada-France-Hawaii Telescope, CNRS, 96743 Kamuela, Hawaii, USA

⁵ Department of Physics & Astronomy, University of Bologna, via Gobetti 93/2, 40129-40129 Bologna, Italy

⁶ Departamento de Astronomia, Instituto de Astronomia, Geofísica e Ciências Atmosféricas da USP, Cidade Universitária, CEP: 05508-900, São Paulo, SP, Brazil

Received 2021 November 12; revised 2022 May 26; accepted 2022 June 11; published 2022 August 9

Abstract

We present the Waves in Nearby Disk galaxies Survey (WiNDS) consisting of 40 nearby low-inclination disk galaxies observed through H_{α} high-resolution Fabry–Perot interferometry. WiNDS consists of 12 new galaxy observations and 28 data archived observations obtained from different galaxy surveys. We derive two-dimensional line-of-sight velocity fields that are analyzed to identify the possible presence of vertical velocity flows in the galactic disks of these low-inclination late-type galaxies using velocity residual maps, derived from the subtraction of an axisymmetric rotation model from a rotational velocity map. Large and globally coherent flows in the line-of-sight velocity of nearby face-on galaxies can be associated with large vertical displacement of the disk with respect to its midplane. Our goal is to characterize how frequent vertical perturbations, such as those observed in the Milky Way, arise in the local universe. Our currently available data have allowed us to identify 20% of WiNDS galaxies with strong velocity perturbations that are consistent with vertically perturbed galactic disks.

Key words: Spiral galaxies – Galaxy kinematics – Galaxy interactions

Supporting material: figure sets

1. Introduction

Over the last ten years, oscillatory perturbations toward the outskirts of the solar neighborhood in the Galactic disk have been reported several times (e.g., López-Corredoira et al. 2002; Momany et al. 2006; Widrow et al. 2012; Slater et al. 2014; Price-Whelan et al. 2015; Xu et al. 2015; Antoja et al. 2018; Collaboration et al. 2021). In particular, using 11k main-sequence stars from the Sloan Digital Sky Survey (SDSS; York et al. 2000) Widrow et al. (2012) detected asymmetries in both, (i) the bulk velocity of solar neighborhood stars associated with a breathing pattern, i.e., compression and rarefaction motions; and (ii) in the vertical stellar number density distribution. The latter was related to a bending pattern, i.e., local displacements of the disk from the midplane (Widrow et al. 2014). This study was followed up by Xu et al. (2015), who analyzed measurements of stellar number counts of main-sequence stars located at Galactic latitudes $110^{\circ} < l < 229^{\circ}$, as a function of Galactocentric radius. They showed that the amplitude of the perturbations in the vertical stellar number counts, i.e., the displacement of the disk with respect to its midplane, increases toward the outskirts of the Galaxy. This type of oscillatory perturbation on the stellar and/or gaseous component of the disk is known as a corrugation pattern. Thanks to the analysis of the full 6D phase-space information for more than six million stars from Gaia Collaboration et al. (2018), Antoja et al. (2018) showed that, indeed, our own Galactic disk is undergoing phase mixing of a nonequilibrium configuration, a perturbation likely associated with the interaction of the Milky

Way with the Sagittarius dwarf galaxy in the past (e.g., Gómez et al. 2013; Laporte et al. 2018b, 2019, 2020, Bland-Hawthorn et al. 2019, Bland-Hawthorn & Tepper-García 2021). More recently, Gaia Collaboration et al. (2021) confirmed that the Milky Way disk has very complex dynamics, with vertical velocity perturbations that can be partially described as a bending wave.

Interestingly, evidence of such complex vertical oscillatory patterns on external galaxies, such as those observed in the Milky Way, is still extremely limited. Vertically perturbed disks have been extensively observed, especially in edge-on galaxies. Studies of 21 cm neutral hydrogen line observations show that most galaxies that have extended HI disks, with respect to the optical, are warped. Using a sample of 26 edge-on galaxies located in different environments with inclinations $i > 75^{\circ}$ and blue diameters larger than $1/5$, from the Westerbork HI Survey of Spiral and Irregular Galaxies (WHISP; van der Hulst et al. 2001), García-Ruiz et al. (2002) showed that all galaxies in their sample with an extended HI disk ($\sim 76\%$) are warped with respect to the optical disk. They also found that warped disk galaxies are more often found in less dense environments, indicating that tidal interactions are not the only mechanism producing galactic warps. However, in denser environments, the disk vertical perturbations typically show larger amplitudes than those in less dense environments. This is likely due to the fact that, in denser environments, galaxies are more likely to undergo violent tidal interactions with companion galaxies.

For observations in optical bands, Ann & Park (2006) analyzed a sample of 325 galaxies from the SDSS, which consists of a majority of late-type spiral galaxies with inclinations $i > 84^{\circ}$ and isophotal major axis length $D_{25} > 1'$ at $\mu_B = 25$ mag arcsec $^{-2}$. The study showed that 73% of the

sample contained a warped disk: 51% corresponds to S-shaped and 22% to U-shaped perturbations. For the analysis of the environment dependence on the frequency of warps, Ann & Park (2006) analyzed 75 galaxies with redshift data from the SDSS DR3, of which 56 have companion galaxies. For the subset of galaxies that have companions, 64% show warped disks. For galaxies without companions, 81% show warped disks. This result is consistent with that presented in García-Ruiz et al. (2002), i.e., in poor environments, a higher frequency of warped disks is found than in rich environments. Vertical perturbations have also been studied in edge-on galaxies using dust lines. Narayan et al. (2020) analyzed a sample of five nearby objects with inclinations $i > 80^\circ$ and also showed that such perturbations are common.

S-shaped warps are expected to be a very common feature of both interacting and isolated late-type galaxies. Gómez et al. (2016, 2017) studied in detail the origin and evolution of vertical perturbation in the disk of late-type galaxies using high-resolution cosmological magnetohydrodynamical simulations of the Auriga Project (Grand et al. 2017). By means of the construction of mass-weighted mean height, $\langle Z \rangle$, and mean vertical velocities maps, $\langle V_z \rangle$, for both the stellar and cold gas components, these studies found that 70% of the Milky Way-like models showed strongly vertically perturbed disks. Interestingly, while only half of the vertically perturbed disks showed integral-sign (S-shaped) warps, the remaining half showed a more complex vertical structure, i.e., corrugation patterns, indicating that such structures are expected to be common.

A possible reason behind the lack of detected vertical patterns relates to the complexity behind their observation. On edge-on galaxies, such a pattern can be easily confused with S-shaped warps due to projection effects. However, as discussed in Gómez et al. (2017), such a corrugation pattern should be detectable along the line-of-sight velocity (V_{los}) of nearby face-on galaxies. Due to the oscillating nature of a corrugation, global patterns on the (V_{los}) field can be directly linked to global patterns in a $\langle Z \rangle$ map. Until recently, previous efforts to detect corrugations in the cold gas disk component of nearby galaxies were based on H_α emission through long-slit spectroscopy. Alfaro et al. (2001) analyzed NGC 5427, a galaxy with an inclination angle of 30° , and found wavy-like variations in the velocity profile of the ionized gas. Sánchez-Gil et al. (2015) analyzed a sample of four spiral galaxies and showed that two presented corrugation patterns. However, due to the limited coverage associated with the long-slit spectroscopic observations, such patterns could be confused with the effects of local perturbations such as fountain flows. In a recent work, Gómez et al. (2021) presented a full 2D velocity map of the low-inclination galaxy, VV304a. Their study was based on Fabry–Perot (FP) interferometer H_α observations. This technique has the great advantage of providing high spectral resolution in a narrow frequency range, along with good spatial resolution (in this work $\sim 2''$). As such, it allows resolving local velocity perturbations with amplitudes of the order of 10 km s^{-1} . The study showed, for the first time, that VV304a presents global and coherent velocity perturbations that are consistent with a corrugation pattern. They also showed that these velocity perturbations cannot be described by the effects associated with the presence of axisymmetric features on its disk, such as the bar and spiral structure. Thus, they conclude that these perturbations are a direct consequence of the gravitational interaction with its similar mass companion galaxy, VV304b.

The characterization of vertical perturbations in nearby disk galaxies can provide very valuable information about their recent interaction with their environment. Several mechanisms could be behind the formation of warps and corrugation patterns (Sellwood 2013; Gómez et al. 2016, 2017). One of them is the tidal distortion of a pre-existing disk by an external perturber, such as the case of our own Milky Way (Antoja et al. 2018; Laporte et al. 2019) and VV304a (Gómez et al. 2021). The strong tidal torques being exerted on a pre-existing disk as relatively massive satellites fly by or merge can induce strong vertical perturbations (Ostriker & Binney 1989; Quinn et al. 1993; Velazquez & White 1999; Bailin 2003; Kazantzidis et al. 2009; Gómez et al. 2013; D’Onghia et al. 2016; Gómez et al. 2017; Laporte et al. 2018a, 2018b). In addition, the torques associated with a non-spherical mass distribution of dark matter can also trigger the formation of vertical patterns (Debattista & Sellwood 1999; Jiang & Binney 1999; Shen & Sellwood 2006; DeBuhr et al. 2012; Yurin & Springel 2015; Gómez et al. 2016; Laporte et al. 2018a). Other possibilities may include misaligned accretion of cold gas due to the cooling of hot gas halo, infalling from the cosmic web, or being left by gas-rich host-satellite interactions (Jiang & Binney 1999; Sancisi et al. 2008; Roškar et al. 2010; Aumer et al. 2013; Radburn-Smith et al. 2014; Gómez et al. 2017) and ram pressure of the surrounding intergalactic material (Haan & Braun 2014). The objective of this work is to search for velocity perturbations in the disks of nearby late-type galaxies. To achieve this goal we use high-resolution observations of near face-on galaxies obtained with an FP interferometer. For this purpose, we present the Waves in Nearby Disk galaxies Survey (WiNDS), which consists of a data set with high spectral resolving power ($R \sim 10000$) and large spatial coverage, making them ideal for investigating the kinematics of the ionized gas in galactic disks. This study is the first step in an effort that aims to characterize the history of interactions of nearby galaxies, and estimate the frequency with which vertical disturbances such as those observed in the Milky Way arise in the local universe.

This paper is organized as follows. In Section 2, we introduce the WiNDS data sample and describe our new observations. In Section 3, we discuss the data reduction procedure. Sections 4 and 5 describe the data analysis and selection and quantification criteria of bending modes. Finally, we present our results in Section 6 and in Section 7 we provide a discussion and our conclusions. In Appendix A, the comments for each individual galaxy and maps of the new observations made in this work are given. The residual velocity maps are shown in Appendix B.1. The rotation curves are displayed in Appendix C.1. In Appendix D.1, the image processing method is described.

2. WiNDS Data Sample

In this section, we present our WiNDS survey, an ongoing observational campaign currently comprising 40 nearby nearly face-on spiral galaxies. WiNDS consists of 12 new observational data and we complement it with additional archival data of 28 late-type galaxies from different surveys. The entire data sample contains 3D data cubes obtained using an FP interferometer with a resolving power at the H_α rest wavelength of $R \approx 10000$. The galaxies in the WiNDS sample were selected according to three main criteria:

1. Distance: Nearby spiral galaxies were selected to have systemic velocities $v \leq 3000 \text{ km s}^{-1}$, corresponding to less than 45 Mpc.
2. Inclination: All galaxies have previously estimated low-inclination angles $i \leq 40^\circ$. Both morphologically and kinematically estimated inclination were considered in this step.
3. Size: All galaxies have projected diameters, a_p , between $2' \leq a_p \leq 4'$.

The goal of this selection criteria is to allow us to resolve velocity perturbations in the observed disks with amplitudes as small as 10 km s^{-1} . In what follows we discuss WiNDS new observations in detail. We also briefly describe the additional surveys utilized to complement WiNDS. In Table 1, we list some of the main properties of the WiNDS sample. The blue histograms in Figure 1 show the distribution of the most relevant parameters for the final WiNDS sample. The solid curves depict the smooth continuous approximation of the underlying histograms. These smooth histograms were obtained using a Gaussian Kernel Density Estimator. The green histograms in the same figure show the parameter distribution of the vertically perturbed galaxy candidates within the WiNDS sample (see Section 5). Although the WiNDS sample is not complete in terms of, e.g., mass and magnitude, it allows performing a first systematic search of vertically perturbed disks in the nearby universe. The 40 selected galaxies span different environments such as clusters, groups, and field galaxies, and a wide variety of morphologies (Sa to Sc). Note, however, that this is an evolving project, and more objects will be added in the future to complement the available sample. Figure 2 shows the optical images of the WiNDS sample, obtained from SDSS DR9 using the g , r , and z bands.

2.1. WiNDS: New Data Cubes

The new observations for WiNDS were obtained using the FP interferometer at the Observatoire de Haute Provence Observatory (OHP, France). In addition to the selection criteria mentioned in Section 2, we focus on galaxies with previously reported H_α observations (James et al. 2004; Sheth et al. 2010). The new data cubes include galaxies with inclination angles ranging from 6° – 33° , except for NGC 2500, which has $i \approx 40^\circ$. The sample contains galaxies with a range of morphological types (between Sa and Sc) and a wide absolute B -band magnitude range ($-17.9 \leq M_B \leq -21.9 \text{ mag}$). It also contains both isolated and interacting galaxies belonging to different environments. The 12 new galaxies observed as part of WiNDS are mainly located in the Northern Hemisphere; a list of the 12 galaxies is reported in Table 1. In particular, NGC 2763 is the only galaxy in our sample observed from the Southern Hemisphere using the SOAR Adaptive Module Fabry–Perot (SAM-FP; Mendes de Oliveira et al. 2017). This galaxy was added to the sample at a later time, based on the availability of the SAM-FP.

2.1.1. WiNDS: Observation of New Data Cubes

Most of the WiNDS observations for the new galaxies were performed in 2019 February using the 1.93 m telescope at the OHP. The observations were made with a mean integration time of 2 hr per galaxy. We note that due to poor weather conditions three galaxies in the sample were observed with a seeing slightly over $3''$.

The new datacubes were obtained through the Gassendi H α survey of Spirals (GHASP) instrument, a focal reducer

containing an FP scanning interferometer, which has a large field of view (FoV) of $\approx 5.9 \times 5.9 \text{ arcmin}^2$, an aperture ratio of $f/3.9$, and a pixel scale $0''.68 \text{ pixel}^{-1}$. The Free Spectral Range (FSR) for the two interferometers used with interference orders of 798 and 2600 are 375.9 and 115.4 km s^{-1} , respectively. The resolving power reached in our survey was $R = 10000 - 28600$, which translates into a velocity resolution of $11.6 - 3.6 \text{ km s}^{-1}$, respectively. As discussed in Gómez-López et al. (2019) the detector, Image Photon Counting System (IPCS), has the advantage of a zero-readout noise, which allows a very fast scan of the interferometer through the entire FSR. The use of an IPCS makes it possible to carry out short exposures (10 s) and to make a large number of cycles (typically 20) to average the variations in observation conditions. Within new observation of WiNDS, the H_α line can be found within the range of $6563 - 6627 \text{ \AA}$. A total of seven filters, each with an FWHM of 15 \AA , are available to isolate the H_α emission line.

For the wavelength calibration of the data, a cube is obtained before and after the observation of each galaxy to account for possible changes in observing conditions. Each calibration cube is obtained using the neon emission line (6598.95 \AA), which is isolated using a narrow-band interference filter ($\sim 15 \text{ \AA}$) centered on this wavelength. This line is used because it is intrinsically narrow and close to the wavelength of the redshifted H_α line.

An additional galaxy, NGC 2763, was observed in 2016 February using the 4.1 m Southern Astrophysical Research (SOAR) telescope, at Cerro Pachón, Chile. The instrument used is the SAM-FP. It is a restricted-use instrument providing a new mode of operation of SAM for spectroscopy using an FP and SAM-Imager (SAMI). The SAM-FP provides an FoV of $\approx 3 \times 3 \text{ arcmin}^2$, a CCD pixel scale of $0''.045 \text{ pixel}^{-1}$ (after electronic binning on the detector), and 48 wavelength channels, in the third dimension of the datacube. For the SAM-FP observations, the interference order was 609 with an FSR of 492.6 km s^{-1} and resolving power of $R = 10000$ which translates into velocity sampling of 10.3 km s^{-1} per channel (for a resolution of $\sim 20.6 \text{ km s}^{-1}$), see Mendes de Oliveira et al. (2017) for more details.

2.2. Additional Data Archive

The new data cubes described in Section 2.1 were complemented with 28 galaxies previously observed, available at the FP interferometer database⁷ and Herschel database⁸ at the Laboratoire d'Astrophysique de Marseille. The galaxies were selected from the GHASP (G), Spitzer Infrared Nearby Galaxies Survey (SINGS)- H_α (S), VIRGO- H_α (V), and Herschel Reference Survey (HRS)- H_α (H) surveys, each of them briefly discussed below. Some basic parameters, describing the corresponding observations, are listed in Table 1.

The data cubes available from the previously mentioned surveys were reprocessed in order to homogenize the galaxy analysis. This was performed considering the same signal-to-noise and smoothing method for all data cubes. Data cubes from the GHASP, VIRGO- H_α , and SINGS- H_α surveys are available in the FP database website (see footnote 1). On the other hand, HRS- H_α data cubes are available in the Herschel Database (see footnote 2).

2.2.1. GHASP Survey

The GHASP (Epinat et al. 2008a, 2008b) survey consists of 3D H_α data cubes of 203 late-type galaxies (spiral and

⁷ <https://cesam.lam.fr/fabryperot/>

⁸ <https://hedam.lam.fr/>

Table 1
WiNDS Galaxy Targets and Data Archive Parameters

NGC	Morph (Type)	t_{morph}	R_{opt} (kpc)	v_{sys} (km s^{-1})	d (Mpc)	M_B (mag)	$v_{\text{rot}}^{\text{max}}$ (km s^{-1})	$\log(M_{\text{star}})$ (M_{\odot})	$\log(M_{\text{HI}})$ (M_{\odot})	\log (SFR)	i ($^{\circ}$)	PA ($^{\circ}$)
(1)	(2)	(3)	(4)	(5)	(6)	(7)	(8)	(9)	(10)	(11)	(12)	(13)
New observations												
628	SAC	5.2	16.4	657.2	10.8	-20.7 ± 0.3	64	10.3 ^a	9.7 ^b	...	7 ^m	252
1058	SAC	5.1	4.3	518.0	9.7	-18.9 ± 0.4	13	...	8.8 ^d	...	6 ^m	152
2500	SBd	7.0	4.5	503.9	10.5	-17.9 ± 1.7	131	9.4 ^a	9.0 ^c	...	40 ^k	86
2763 (SAM-FP)	SBcd	9.9	10.0	1891.6	29.6	-19.8 ± 0.3	117	30 ^k	50
3147	SABc	3.9	26.1	2801.9	46.1	-21.9 ± 0.2	335	11.4 ^a	32 ^m	147
3184	SABcd	5.9	11.4	592.1	10.9	-19.1 ± 0.4	208	10.4 ^a	9.3 ^c	...	16 ^k	1
3423	SACd	6.0	8.5	1004.0	15.2	-20.0 ± 0.2	128	9.7 ^a	9.1 ^b	...	19 ^k	45
3485	SBb	3.2	9.4	1436.0	28.2	-19.1 ± 0.8	188	9.9 ^a	9.3 ^b	0.6 ^e	20 ^k	116
3642	SABc	4.0	23.3	1588.0	30.0	-20.6 ± 0.6	48	10.4 ^a	25 ^k	123
4136	SABc	5.2	4.2	608.9	7.2	-18.5 ± 1.5	102	9.5 ^a	8.9 ^b	...	22 ^k	72
4900	SBc	5.1	3.2	959.6	9.8	-19.2 ± 1.1	112	10.4 ^a	9.1 ^b	...	5 ^k	0
5194	SABc	4.0	15.8	462.9	9.8	-21.3 ± 0.3	134	10.9 ^a	9.3 ^c	...	20 ^k	13
Data archive												
864 (G)	SABc	5.1	15.3	1561.9	22.6	-19.9 ± 0.4	134	10.2 ^a	9.6 ^b	...	35 ^k	27
2775 (G)	SAab	1.6	14.3	1350.0	23.0	-20.6 ± 0.8	296	10.9 ^a	8.6 ^b	...	38 ^k	157
3344 (G)	SABbc	4.0	7.7	580.1	7.4	-19.6 ± 0.3	217	9.7 ^a	9.6 ^b	...	18 ^k	156
3346 (G)	SBcd	5.9	10.3	1274.1	24.5	-19.1 ± 0.9	126	10.2 ^a	9.1 ^b	0.6 ^e	34 ^m	113
3351 (S)	SBb	3.1	10.5	777.9	9.7	-19.8 ± 0.1	151	10.5 ^a	9.0 ^b	...	40 ^k	11
3504 (G)	SABab	2.1	11.7	1525.0	29.8	-20.5 ± 0.7	194	10.4 ^a	8.8 ^b	3.6 ^e	39 ^k	164
3596 (G)	SABc	5.2	14.0	1192.9	24.2	-19.7 ± 0.9	157	10.0 ^b	9.0 ^b	...	17 ^k	77
3631 (H)	SAC	5.1	17.3	1155.9	23.8	-21.0 ± 0.8	79	10.2 ^a	...	2.7 ^e	24 ^k	171
3938 (S)	SAC	5.1	12.9	809.1	16.6	-20.1 ± 1.1	128	10.5 ^a	9.3 ^d	...	8 ^k	17
4037 (H)	SBb	3.3	5.5	932.1	15.1	-18.0 ± 0.1	101	9.7 ^a	8.5 ^b	0.2 ^e	32 ^k	151
4189 (V)	SABcd	5.9	5.3	2115.0	15.1	-19.7 ± 0.5	196	10.5 ^a	9.4 ^b	...	31 ^k	70
4321 (V)	SABbc	4.0	16.3	1570.9	15.1	-21.2 ± 0.1	279	10.9 ^a	9.4 ^b	6.2 ^e	38 ^k	149
4411B (H)	SABcd	6.2	5.5	1272.0	14.9	-19.4 ± 0.2	76	9.5 ^a	9.0 ^b	...	18 ^k	52
4430 (H)	SBb	3.5	4.9	1451.0	14.7	-20.3 ± 0.5	87	9.8 ^a	8.6 ^b	0.7 ^e	28 ^m	60
4519 (V)	SBd	6.9	6.9	1218.1	14.8	-19.3 ± 0.2	117	10.2 ^a	9.5 ^b	0.9 ^e	40 ^k	180
4625 (S)	SABm	8.7	3.6	620.9	11.3	-17.9 ± 1.3	39	9.1 ^a	8.5 ^c	...	36 ^k	126
4725 (S)	SABab	2.2	45.0	1206.1	28.8	-20.7 ± 0.2	257	10.9 ^a	9.6 ^b	1.6 ^e	30 ^m	28
4736 (S)	SAab	2.3	8.4	307.9	5.2	-19.7 ± 0.3	182	10.5 ^a	8.3 ^c	...	36 ^k	118
5204 (G)	SAM	8.9	4.4	200.9	5.9	-17.0 ± 0.1	56	8.7 ^a	8.6 ^c	...	40 ^k	17
5334 (H)	SBc	5.3	15.9	1385.9	26.1	-19.1 ± 1.1	133	10.4 ^a	9.1 ^c	0.5 ^e	38 ^k	6
5430 (G)	SBb	3.1	16.1	2961.1	50.5	-20.8 ± 0.4	188	10.7 ^a	32 ^k	8
5585 (G)	SABd	6.9	7.1	292.9	8.2	-18.7 ± 0.2	79	9.3 ^a	8.8 ^c	...	36 ^k	50
5668 (G)	SAd	6.9	14.3	218.4	29.7	-20.1 ± 0.6	73	10.2 ^a	9.9 ^b	1.6 ^e	18 ^k	146
5669 (H)	SABcd	6.0	15.8	1367.9	27.3	-18.6 ± 0.7	102	10.2 ^a	9.3 ^b	1.0 ^e	36 ^m	71
5713 (S)	SABbc	4.0	13.5	1898.9	33.8	-21.2 ± 0.5	108	10.6 ^a	33 ^k	23
6217 (G)	SBbc	4.0	11.4	1362.0	26.1	-20.5 ± 0.7	113	10.5 ^a	9.6 ^c	...	34 ^k	105
6946 (G)	SABcd	5.9	10.0	39.9	5.9	-20.9 ± 0.2	315	...	9.9 ^c	...	17 ^m	61
UGC 3685 (G)	SBb	3.0	14.6	1797.0	30.3	-19.9 ± 0.6	41	...	9.8 ^c	...	12 ^k	134

Note. (1) Galaxy name in the NGC catalog, except for UGC 3685, which does not have an NGC name; the letter in parenthesis corresponds to the survey name: (G) for GHASP (Epinat et al. 2008a, 2008b), (S) for SINGS (Daigle et al. 2006a; Dicaire et al. 2008), (V) for Virgo (Chemin et al. 2006), and (H) for HRS (Gómez-López et al. 2019); (2) and (3) morphological type found in the HyperLeda database; (4) optical radius considering the isophotal radius at the limiting surface brightness of 25 B mag arcsec⁻² from the Third Reference Catalog of Bright Galaxies (RC3; de Vaucouleurs et al. 1991) corrected for the Virgo and Great Attractor (GA) infall, assuming $H_0 = 67.8 \text{ km s}^{-1} \text{ Mpc}^{-1}$; (5) systemic velocity from NED; (6) distance in megaparsec from NED, corrected for the Virgo and GA infall, assuming $H_0 = 67.8 \text{ km s}^{-1} \text{ Mpc}^{-1}$; (7) absolute B -band magnitude (HyperLeda); (8) maximum rotation velocity corrected for inclination from HyperLeda; (9) stellar mass a from Sheth et al. (2010); (10) H I mass b from Haynes et al. (2018), c from Karachentsev et al. (2013), d from the radio survey Westerbork survey of H I in SPirals (WHISP) galaxies <https://www.astro.rug.nl/~whisp/>; (11) star formation rate. e from Boselli et al. (2015); (12) inclinations k correspond to kinematic values and m correspond to morphological values from the literature; and (13) PA.

irregular). This sample contains a wide range of morphological types, from Sa to Irr, with absolute magnitudes in the range of $-16 \leq M_B \leq -22$ mag, stellar masses ranging from $10^9 - 5 \times 10^{11} M_{\odot}$ and are located in nearby low-density environments. From the total sample of 203 galaxies, 83 are strongly barred galaxies (SB or IB) and 53 moderately barred galaxies (SAB or IAB). According to our selection criteria described in Section 2, 13 galaxies were selected and are reported in Table 1.

2.2.2. SINGS- H_{α} Survey

The legacy SINGS (Kennicutt et al. 2003) consists of 75 nearby galaxies selected with a wide coverage of morphological type (E to Im), luminosity types (IR quiescent to luminous IR galaxies), and CO/HI ratio covering over 3 orders of magnitudes. These galaxies are located in different environments such as galaxy groups, clusters, and low-density fields. The SINGS survey was created to characterize the infrared emission in a wide range of galaxy properties and star

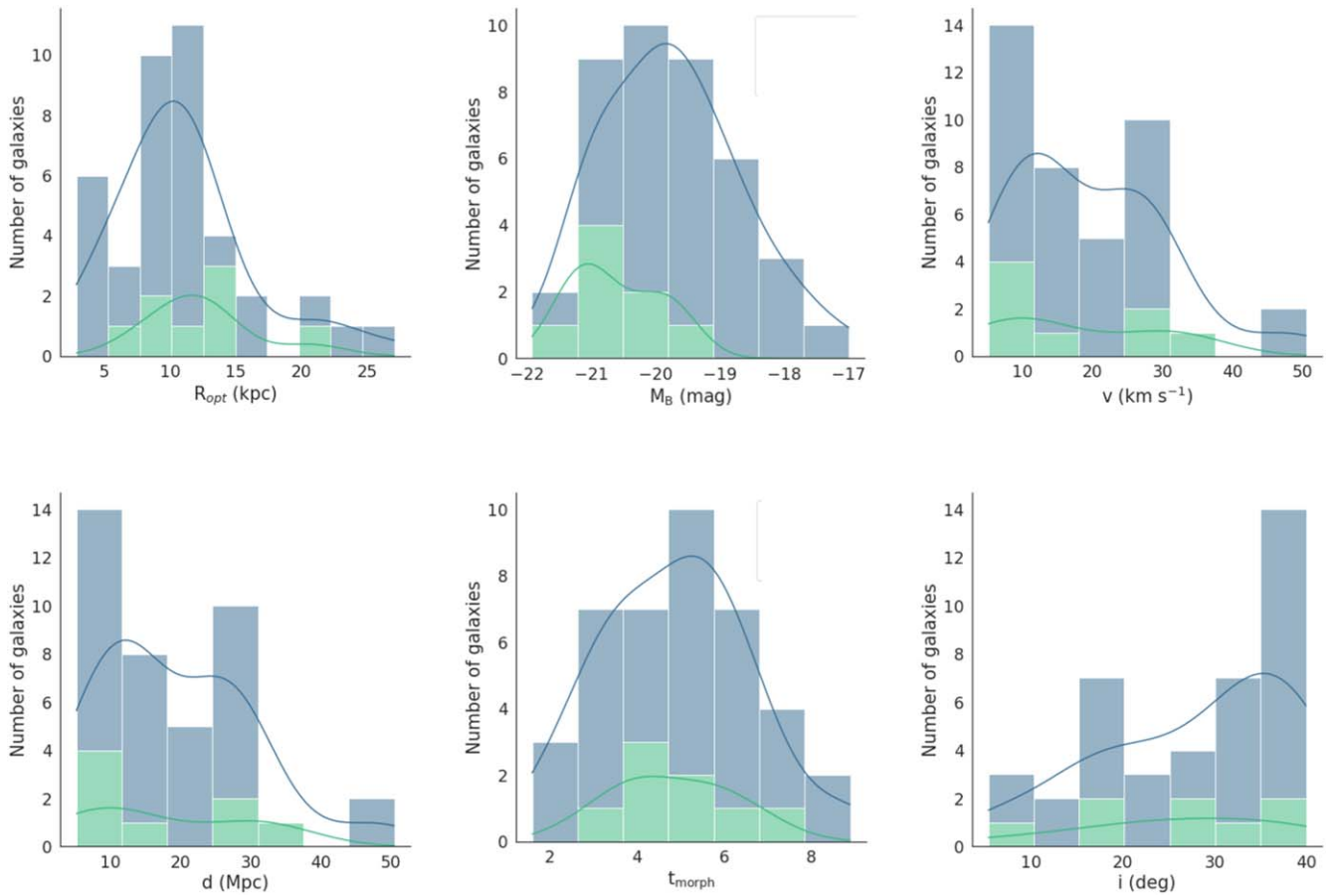


Figure 1. Basic parameter distributions for our sample of 40 WiNDS galaxies. Top left: optical radius distribution at 25 mag arcsec⁻² corrected for the effects of projection and extinction. Top middle: absolute B -band magnitudes. Top right: radial velocity distribution. Bottom left: distribution of distances in Mpc (corrected for the Virgo, Great Attractor, and Shapley supercluster infall). Bottom middle: galaxy type distribution. Bottom right: inclination angles distribution. The solid line corresponds to the smooth continuous approximation of the underlying distribution. The blue distributions correspond to the total sample of WiNDS galaxies, while the green distributions correspond to the vertically perturbed galaxy candidates.

formation environments. The SINGS- H_α data is an H_α kinematic follow-up survey of SINGS (Daigle et al. 2006a; Dicaire et al. 2008) and consists of 65 late-type galaxies that present HII regions. According to the criteria described in Section 2, the selected galaxies are reported in Table 1.

2.2.3. VIRGO- H_α Survey

The 3D H_α data cubes from the Virgo survey, VIRGO H_α , (Chemin et al. 2006) consist of 30 spiral and irregular galaxies. This survey is a subsample of the Virgo Cluster Catalog (Binggeli et al. 1985, 1993), which is the nearest cluster to the Milky Way and has ~ 1400 members, mainly dwarf-type galaxies. The galaxies considered in the VIRGO- H_α survey have an apparent magnitude greater than $B_r^0 = 12$ mag, wide morphological types (S0/a to Im), and inclination angles between 25° and 89° . All galaxies are located in the cluster’s core and its extension is toward M49. According to our criteria selection described in Section 2, the three selected galaxies are reported in Table 1.

2.2.4. HRS- H_α Survey

The HRS- H_α survey (Gómez-López et al. 2019) consists of 152 star-forming galaxies observed using the 1.93 m telescope at the OHP. This survey aimed to study the relationship between the baryonic and dynamical mass of galaxies. The

HRS- H_α galaxies sample spans a wide range of morphologies (from Sa to Sm types, including blue compact dwarfs) and stellar masses ($10^8 M_\odot \leq M_{\text{star}} \leq 10^{11} M_\odot$).

From the HRS- H_α sample, and excluding overlap with previous surveys (GHASP, SINGS H_α , and VIRGO H_α), we found seven galaxies that follow our selection criterion. The names of the six targets are listed in Table 1.

Note that not all of the galaxies come from the same source. Table 2 shows our observations broken down by instrument, telescope, survey of origin, and number of galaxies observed. The most relevant observational parameters are listed in Table 3. For completeness, in the same table we also list the properties of the additional observations extracted from the data archive.

3. WiNDS: Data Reduction

The WiNDS data sample was reduced using the pipeline-based program COMPUTEVERYTHING⁹ and the REDUCWIZARD¹⁰ interface, following the steps described in Daigle et al. (2006b) and Epinat et al. (2008b).

The data reduction process includes (a) the wavelength calibration, (b) the night-sky lines subtraction, (c) the

⁹ <https://projets.lam.fr/projects/computeeverything>

¹⁰ <https://projets.lam.fr/projects/freducwizard>

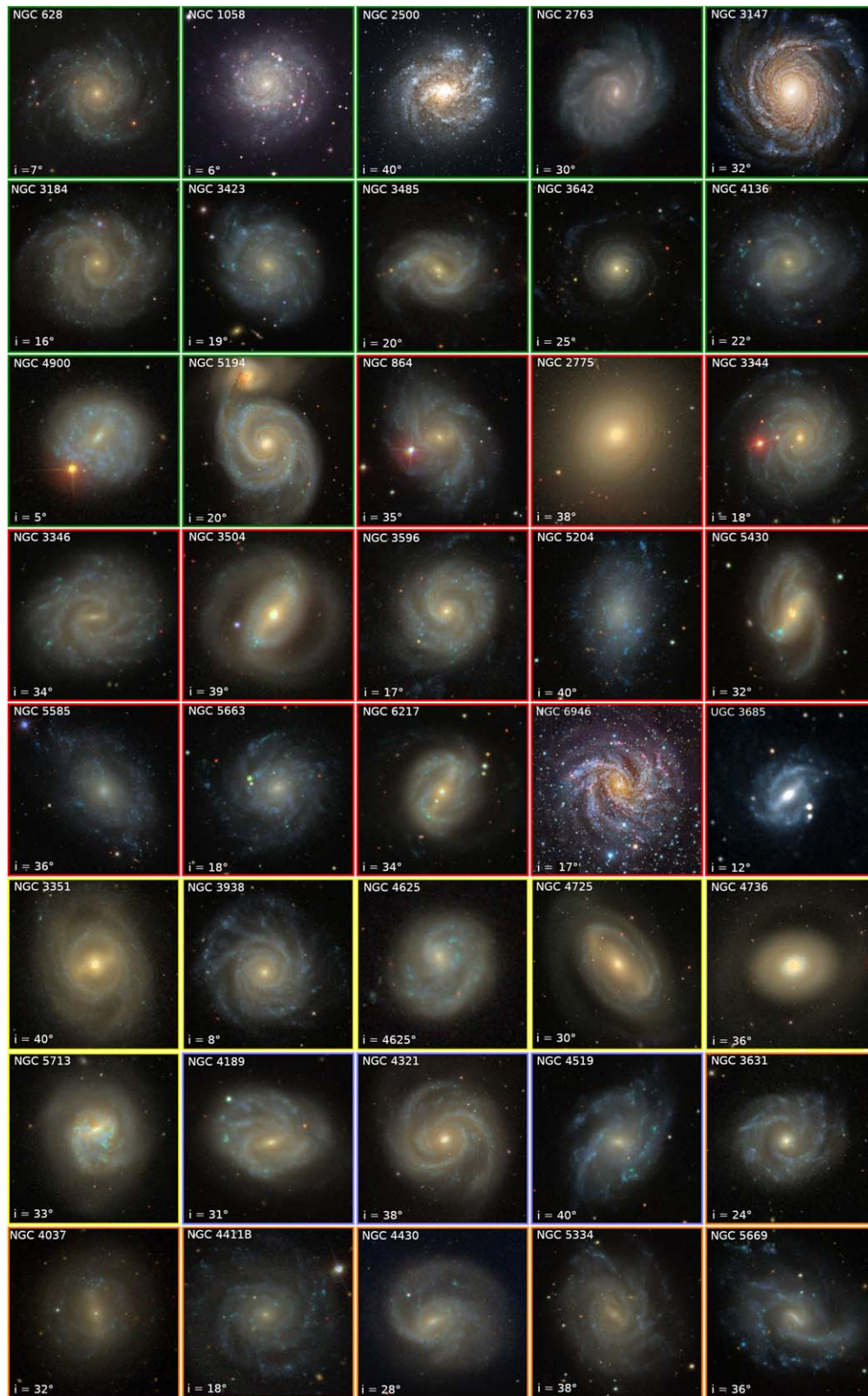


Figure 2. Optical images of WiNDS galaxies from SDSS: new observations (green outline); GHASP (red outline); SINGS (yellow outline); VIRGO survey (blue outline), and HRS (orange outline).

astrometry process, (d) the adaptive spatial binning using the 2D Voronoi tessellation, whose implementation finally produces a smoothing specially adapted to a given signal-to-noise ratio (S/N),

(e) the generation of the 2D momentum maps, (f) a semiautomatic cleaning of the velocity fields, and (g) velocity dispersion correction. In the following we briefly describe these processes:

Table 2
Setup

Instrument (1)	Telescope (2)	Galaxies (3)	Survey (4)
GHASP	OHP	30	WiNDS, GHASP, HRS
Cigale	ESO	1	Virgo
FANTOMM	OMM/ESO/CFHT	8	SINGS, Virgo
SAM-FP	SOAR	1	WiNDS

Note. (1) Instrument, (2) telescope, (3) number of galaxies observed for each instrument, and (4) survey name. OMM: Observatoire du mont Mégantic, Québec, Canada, 1.6 m telescope; ESO: European Southern Observatory, La Silla, Chile, 3.6 m telescope; CFHT: 3.6 m Canada–France–Hawaii Telescope, Hawaii, USA.

- (a) The calibration process consists of applying a phase map to provide the same wavelength/velocity origin to each profile, for each pixel of the observation datacube. The 2D phase map is computed from the two calibration datacubes. During the phase correction process, the individual exposures are recentered with respect to each other, using field stars, to minimize telescope drifts and instrument bend.
- (b) The OH emission lines are the main foreground sky contamination. The sky subtraction is done by dividing the collapsed datacube into a galaxy-dominant and a sky-dominant region. The night-sky emission is interpolated from this galaxy-free region using a two-degree polynomial, and subsequently removed from the whole datacube.
- (c) The next step is astrometry, which is done through the KOORDS task in the KARMA¹¹ package (Gooch 1996), comparing star fields between XDSS¹² R -band images and our continuum images of each galaxy.
- (d) For the estimation of the S/N, which is related to the flux in the line, to the spectral resolution and the rms in the continuum, we use adapted spatial binning through Voronoi tessellation, as described in Daigle et al. (2006b). This allows us to obtain the highest spatial resolution for a given S/N, which is the main advantage of this binning technique. The Voronoi bins are constructed iteratively from a given pixel, by accreting adjacent pixels until the resulting spectrum reaches the desired S/N. Pixels where the S/N is greater than the chosen threshold value will not be affected by the binning process, while regions of low S/N will emerge from noise without being contaminated by adjacent regions of higher S/N. For the WiNDS sample, the objective is to obtain an $S/N \geq 7$ per spatial bin, where S/N is considered as the square root of the flux in the line. We implemented a Hanning smoothing of a one-spectral element of the spectrum, which preserves the flux.
- (e) From this Voronoi binned datacube, the different momentum maps are computed as explained in Daigle et al. (2006b): after identifying the H_α line boundaries, the continuum emission around the line is estimated and subtracted from the spectrum. The moments of the line are then estimated. Namely, the line or monochromatic flux is the zeroth-order moment (intensity integrated within the line boundaries), the line-of-sight velocity (V_{los}) is the

first-order moment (intensity-weighted velocity sum within the line boundary), and the line-of-sight velocity squared velocity dispersion (variance) as the second-order moment (difference between the intensity-weighted squared velocity and squared intensity-weighted velocity within the line boundaries).

- (f) In some cases, the lowest S/N regions are strongly affected by night-sky line contamination. Thus, a semiautomatic cleaning is performed. Indeed, to achieve the desired S/N in the outermost galactic regions very large Voronoi bins are produced. These are mainly associated with sky subtraction residuals and background emission. Those bins are first semiautomatically erased and then manually deleted when the semiautomatic process is not sufficient.
- (g) Finally, velocity dispersion maps were corrected by instrumental width. This correction was done by subtracting the mean dispersion of the instrument contribution to the observed velocity dispersion map, as follows:

$$\sigma_{\text{corr}} = \sqrt{\sigma_{\text{obs}}^2 - \sigma_{\text{inst}}^2}, \quad (1)$$

where σ_{obs} corresponds to the observed velocity dispersion and σ_{inst} is the mean dispersion of the instrument contribution. Moreover, σ_{inst} is a function of the FSR, the interference order p , and the resolving power R :

$$\sigma_{\text{inst}} = \frac{\text{FSR } p}{R}. \quad (2)$$

The results of the data reduction process are presented below for a WiNDS subsample where panels (a)–(c) show the XDSS B -band image, the H_α line-of-sight velocity map, and the H_α velocity dispersion map, respectively. In addition, the results of the data reduction for the remaining new observations made in this work, where the XDSS blue image (top left panel), the H_α monochromatic image (top right panel), H_α velocity field (bottom left panel), and the H_α residual velocity field (bottom right panel) are shown in Appendix A.2.

4. Residual Velocity Fields

Our goal is to analyze the previously derived line-of-sight velocity map, V_{los} , to search for evidence of large, global, and coherent kinematic perturbations on our sample of late-type, low-inclination galaxies. In particular, we seek perturbations that are consistent with bending modes produced by warps and corrugation patterns. In this section, we discuss the procedure followed to analyze our resolved velocity fields.

As discussed in Gómez et al. (2021), the observed V_{los} field of each galaxy is bound to contain contributions from three different velocity components: the distributions within the disk plane, radial V_R and rotational, V_{rot} , and the perpendicular velocity to the disk plane, V_Z . More precisely, each V_{los} can be described as

$$\begin{aligned} V_{\text{los}} = & V_{\text{sys}}(r) + V_{\text{rot}}(r)\cos\theta\sin i \\ & + V_R(r)\sin\theta\sin i \\ & + V_Z(r)\cos i, \end{aligned} \quad (3)$$

where V_{sys} is the systemic velocity of the galaxy and it is considered a fixed value. The polar coordinates (r , θ) in the plane of the galaxy are measured from the position angle (PA),

¹¹ KARMA tools package is available at <https://www.atnf.csiro.au/computing/software/karma/>.

¹² ESO Online Digitized Sky Survey <https://archive.eso.org/dss/dss>.

Table 3
WiNDS Log

NGC	UGC	R.A.	Decl.	Cube	Pixel scale	Int Order	Date	λ_{scan}	R	Seeing
(1)	(2)	(hh mm ss)	($^{\circ}$ ' ")	xyz	(arcsec)	(7)	(yyyy-mm-dd)	(\AA)	(10)	(arcsec)
(1)	(2)	(3)	(4)	(5)	(6)	(7)	(8)	(9)	(10)	(11)
New observations										
628	1149	01 36 41.8	15 47 00	512 512 32	0.68	2600	2019-02-05	6577.2	28600	*
1058	2193	02 43 30.1	37 20 28	512 512 32	0.68	798	2019-02-03	6574.2	10000	**
2500	4165	08 01 53.2	50 44 14	512 512 32	0.68	798	2019-02-04	6573.8	10000	**
2763 (SAM-FP)		09 06 49.1	-15 29 59	1024 1028 48	0.045	609	2016-02-18	6604.2	10000	*
3147	5332	10 16 53.7	73 24 03	512 512 32	0.68	798	2019-02-08	6624.1	10000	**
3184	5557	10 18 16.9	41 25 28	512 512 32	0.68	2600	2019-02-05	6575.8	28600	**
3423	5962	10 51 14.3	05 50 24	512 512 32	0.68	2600	2019-02-07	6584.8	28600	**
3485	6077	11 00 02.4	14 50 29	512 512 32	0.68	798	2019-02-03	6574.2	10000	**
3642	6385	11 22 17.9	59 04 28	512 512 32	0.68	2600	2019-02-06	6597.6	28600	**
4136	7134	12 09 17.7	29 55 39	512 512 32	0.68	2600	2019-02-06	6576.1	28600	**
4900	8116	13 00 39.2	02 30 03	512 512 32	0.68	798	2019-02-04	6583.8	10000	**
5194	8493	13 29 52.7	47 11 42	512 512 32	0.68	2600	2019-02-06	6572.9	28600	*
Data Archive										
864 (G)	1736	02 15 27.6	06 00 09	512 512 24	0.68	793	2000-10-23	6597.0	≈ 10000	**
2775 (G)	4820	09 10 20.1	07 02 17	512 512 24	0.68	793	2003-03-06	6592.4	≈ 10000	**
3344 (G)	5840	10 43 31.2	24 55 20	512 512 24	0.68	793	2002-03-20	6575.5	≈ 10000	**
3346 (G)	5842	10 43 38.9	14 52 19	512 512 24	0.68	793	2004-03-20	6590.7	≈ 10000	**
3351 (S)	5850	10 43 57.7	11 42 13	512 512 48	1.61	765	2005-02-03	6579.8	13750	***
3504 (G)	6118	11 03 11.2	27 58 21	512 512 24	0.68	793	2002-03-18	6596.2	≈ 10000	**
3596 (G)	6277	11 15 06.2	14 47 13	512 512 24	0.68	793	2004-03-19	6588.9	≈ 10000	**
3631 (H)	6360	11 21 02.9	53 10 10	512 512 32	0.68	798	2016-02-03	6587.3	≈ 10000	***
3938 (S)	6856	11 52 49.5	44 07 15	512 512 48	1.61	765	2004-03-11	6579.7	12852	***
4037 (H)	7002	12 01 23.7	13 24 04	512 512 32	0.68	798	2016-02-15	6582.4	≈ 10000	***
4189 (V)	7235	12 13 47.3	13 25 29	512 512 24	0.68	793	2003-03-07	6609.1	7950	**
4321 (V)	7450	12 22 54.8	15 49 19	512 512 52	1.61	899	2003-02-25	6597.2	21000	**
4411B (H)	7546	12 26 47.2	08 53 05	512 512 32	0.68	798	2016-02-04	6589.0	≈ 10000	***
4430 (H)	7566	12 27 26.4	06 15 46	512 512 32	0.68	798	2016-02-15	6593.7	≈ 10000	***
4519 (V)	7709	12 33 30.3	08 39 17	512 512 48	1.61	899	2003-04-04	6589.5	21000	*
4625 (S)	7861	12 41 52.7	41 16 26	512 512 48	0.48	899	2003-04-06	6576.4	14294	***
4725 (S)	7989	12 50 26.6	25 30 03	512 512 48	1.61	765	2004-02-19	6589.2	14305	***
4736 (S)	7996	12 50 53.1	41 07 14	512 512 48	1.61	765	2005-05-11	6569.6	12745	***
5204 (G)	8490	13 29 36.5	58 25 07	256 256 24	0.68	793	...	6567.2	≈ 10000	**
5334 (H)	8790	13 52 54.5	-01 06 53	512 512 32	0.68	798	2018-12-07	6592.1	≈ 10000	***
5430 (G)	8937	14 00 45.7	59 19 42	512 512 24	0.96	897	2003-03-03	6627.6	≈ 10000	**
5585 (G)	9179	14 19 48.2	56 43 45	512 512 24	0.68	793	2004-03-20	6569.2	≈ 10000	**
5668 (G)	9363	14 33 24.3	04 27 02	512 512 24	0.68	793	2003-04-26	6597.3	≈ 10000	**
5669 (H)	9353	14 32 43.5	09 53 26	512 512 32	0.68	798	2016-02-16	6591.9	≈ 10000	***
5713 (S)	9451	14 40 11.5	-00 17 20	512 512 24	0.42	609	2004-04-13	6604.4	5785	***
6217 (G)	10470	16 32 39.2	78 11 53	512 512 24	0.68	793	...	6592.6	≈ 10000	**
6946 (G)	11597	20 34 52.3	60 09 14	512 512 24	0.68	793	2002-06-14	6563.7	≈ 10000	**
	3685	07 09 05.9	61 35 44	512 512 24	0.68	793	2002-03-17	6602.1	≈ 10000	**

Note. (1) Galaxy name in the NGC catalog, except for UGC 3685, which does not have an NGC name; the letter corresponds to the survey name, (2) name of the galaxy in the UGC catalog when available, (3–4) R.A. and decl. (J2000), (5) cube dimension: x (right ascension α), y (decl. δ), and z (number of channels), (6) pixel scale, (7) interference order (at the H_{α} rest wavelength), (8) date of the observation, (9) scanning wavelength, (10) spectral resolution ($\Delta\lambda/\lambda$) according to the computed finesse, (11) * is for a seeing $<2''$, ** is for a seeing between $2''$ and $4''$, *** see papers (H) (Gómez-López et al. 2019) and (S) (Daigle et al. 2006b; Dicaire et al. 2008).

inclination (i), and sky position (α , δ) of the rotation center. The first step in identifying global perturbations in the data is to subtract from the V_{los} map an axisymmetric model of V_{rot} . To obtain such an axisymmetric velocity model we assume that, at first order, the contributions from the radial and the vertical velocities to V_{los} are negligible. Therefore, the observed velocity Equation (3) reduces to

$$V_{\text{los}} = V_{\text{sys}}(r) + V_{\text{rot}}(r) \cos \theta \sin i. \quad (4)$$

To obtain $V_{\text{rot}}(R)$, we use the tilted-ring method (Bege-man 1987), which assumes that the galaxy can be analyzed

using concentric rings along the major axis, which are described by the parameters V_{rot}^r , i^r , PA^r . Here, the supra index r indicates that we are referring to the rings. In this work, we use an improved tilted-ring method, described in detail in Epinat et al. (2008b), and derive $V_{\text{rot}}(R)$ for each galaxy bin modeled using the modified Zhao function (Epinat et al. 2008b),

$$V_{\text{rot}}(r) = v_t \frac{(r/r_t)^g}{1 + (r/r_t)^a}. \quad (5)$$

This four-parameter model was especially chosen for its versatility to adjust to a very diverse set of different rotation curve

shapes. The four parameters involved in the V_{rot} model are v_t and r_t , which correspond to the velocity and radius when the rotation curve changes from an increasing velocity to a flat regime, respectively; a and g , which are related to the sharpness of the turnover. As discussed in Epinat et al. (2008b), for each galaxy the fitting procedure requires a set of initial values for the Zhao function parameters as well as for (α, δ) , i , and PA. In our work, the values of (α, δ) are set to the peak of the emission in the continuum image and set as fixed values. For the systemic velocity, PA, and i , initial values were extracted from the literature. The resulting values of i and PA, obtained as a result of the fitting procedure, are referred to as kinematically inferred values. Note that, in those cases where disks are projected nearly perfectly face-on ($i < 10^\circ$), the value of i is not allowed to vary, and thus, is kept fixed to their estimated morphological value. Instead, the v_t , r_t , a , and g parameters are always allowed to vary. Finally, V_{rot} for each Voronoi binning is estimated through the minimization of χ^2 based on the Levenberg–Marquardt method (Press et al. 1992), computing an iterative 3.5σ clipping on the observed bin-centroid velocity field. All kinematical parameters (i_k , PA_k , and V_{sys}) estimated for the WiNDS galaxies are listed in Table 4. The estimation of errors in the determination of kinematic parameters for the WiNDS sample was calculated using the power spectrum of the residual velocity field and the application of a Monte Carlo method, as described in more detail in Epinat et al. (2008b). It is worth noting that the degeneracy between V_{max} and i when fitting our models (Begeman 1989), is especially for very low-inclination disks, does not affect our results as we are focusing our analysis on the residual velocity fields, V_{res} . The H_α V_{max} values derived in this work are listed in Table 4.

Once an unperturbed axisymmetric model of V_{los} is obtained for each galaxy, we generate their corresponding V_{res} fields. This is done by subtracting the properly V_{los} model from the observed V_{los} maps. It is worth recalling that global and coherent features in a V_{res} field of a late-type galaxy could be the result of kinematic perturbations induced by features such as a bar or spiral structures, but also from improper model parameters (such as center, systemic velocity, PA of the major axis, inclination, or rotation curve model). The multipolar signatures expected for ill-defined parameters (Warner et al. 1973) are not observed in our data.

It is also worth noting that small variations in the magnitude of V_{res} could be attributed to uncertainties in the determination of the kinematic parameters (PA and center). In order to verify the sensitivity of the method used to the initially chosen and fixed inclination value, the model is rerun considering the extreme values of the inclination that are within the error range shown in Table 4.

The contributions from in-plane flows are expected to be small in low-inclination galaxies such as those studied in this work. Using a suite of numerical simulations, Gómez et al. (2021) characterized the contribution from in-plane flows to the V_{los} driven by non-axisymmetric structures. Their models consisted of a disk galaxy, projected into an inclination of 35° , considering a bar with similar characteristics to that of the Milky Way and spiral overdensities that ranged from 100%–1000% density contrast ($\Delta\rho/\rho$) with respect to the disk background density. Even for $\Delta\rho/\rho=1000$ the resulting velocity perturbations in the corresponding V_{res} field were $\lesssim 10 \text{ km s}^{-1}$.

Table 4
Model Parameters

ID	i_k ($^\circ$)	PA_k ($^\circ$)	V_{sys} (km s^{-1})	$v_{\text{rot}}^{\text{max}}$ (km s^{-1})
(1)	(2)	(3)	(4)	(5)
New observations				
NGC 628	7*	155 ± 2	658 ± 1	147
NGC 1058	6*	34 ± 2	521 ± 0	140
NGC 2500	41 ± 11	85 ± 2	512 ± 1	49
NGC 2763	30 ± 8	47 ± 1	1884 ± 1	123
NGC 3147	32 ± 20	37 ± 8	2894 ± 3	164
NGC 3184	16 ± 9	5 ± 1	592 ± 0	155
NGC 3423	40 ± 8	134 ± 1	1007 ± 1	76
NGC 3485	30 ± 7	156 ± 2	1428 ± 1	146
NGC 3642	36 ± 8	70 ± 8	1581 ± 1	72
NGC 4136	20 ± 6	108 ± 1	606 ± 1	82
NGC 4900	5*	80 ± 2	959 ± 1	297
NGC 5194	20 ± 11	13 ± 2	464 ± 2	189
Data archive				
NGC 864 (G)	35 ± 18	30 ± 3	1525 ± 3	52
NGC 2775 (G)	38 ± 3	157 ± 0	1350 ± 1	262
NGC 3344 (G)	15 ± 11	153 ± 2	580 ± 1	262
NGC 3346 (G)	29 ± 8	113 ± 2	1245 ± 1	95
NGC 3351 (S)	21 ± 5	169 ± 1	781 ± 1	289
NGC 3504 (G)	39 ± 13	160 ± 3	1523 ± 2	100
NGC 3596 (G)	17 ± 12	78 ± 2	1190 ± 2	87
NGC 3631 (H)	24 ± 14	151 ± 2	1150 ± 2	59
NGC 3938 (S)	14 ± 8	164 ± 1	809 ± 0	143
NGC 4037 (H)	32 ± 20	151 ± 3	924 ± 1	50
NGC 4189 (V)	31 ± 11	169 ± 1	2102 ± 1	128
NGC 4321 (V)	25 ± 9	29 ± 1	172 ± 1	190
NGC 4411B (H)	18 ± 15	49 ± 3	1267 ± 1	37
NGC 4430 (H)	28 ± 13	75 ± 2	1424 ± 1	180
NGC 4519 (V)	40 ± 16	180 ± 4	1216 ± 2	124
NGC 4625 (S)	8 ± 12	124 ± 3	626 ± 1	105
NGC 4725 (S)	43 ± 4	156 ± 1	1198 ± 2	227
NGC 4736 (S)	25 ± 7	122 ± 1	318 ± 1	245
NGC 5204 (G)	40 ± 11	166 ± 1	186 ± 1	87
NGC 5334 (H)	38 ± 4	6 ± 1	1402 ± 7	105
NGC 5430 (G)	32 ± 8	2 ± 1	2963 ± 3	255
NGC 5585 (G)	36 ± 20	53 ± 3	298 ± 2	59
NGC 5668 (G)	18 ± 14	146 ± 2	1575 ± 1	94
NGC 5669 (H)	36 ± 9	65 ± 1	1377 ± 1	116
NGC 5713 (S)	12 ± 12	154 ± 3	1896 ± 1	84
NGC 6217 (G)	18 ± 10	104 ± 1	1356 ± 1	207
NGC 6946 (G)	17 ± 14	61 ± 2	38 ± 2	185
UGC 3685 (G)	12 ± 19	118 ± 10	1815 ± 3	25

Note. (1) Galaxy name, the letter corresponds to the survey name; (2) kinematic inclination, those marked with an asterisk (*) have been fixed equal to morphological value, (3) kinematic PA, (4) systemic velocity, and (5) maximum rotation H_α velocity corrected for inclination derived in this work.

5. Quantification and Selection Criteria of Bending Modes

In this section, we describe the selection criteria applied to select those galaxies within the WiNDS sample that show velocity perturbations consistent with a bending mode, such as a warp or corrugation pattern. To avoid selecting discrete and local vertical perturbations, such as those associated with, e.g., fountain flows, we have established the main criteria to select strong candidates as follows:

1. We focus on galaxies that present an extended H_α coverage, extending for at least $0.7 R_{\text{opt}}$. This criterion allows us to globally explore the kinematics of the disks,

especially in the outer regions where bending modes typically show their stronger amplitudes.

2. We focus on galaxies where global perturbations show amplitudes that are $>10 \text{ km s}^{-1}$. This enhances the chances that the observed perturbations in this low-inclination sample of disks are not mainly driven by the axisymmetric components of the galaxies.
3. We applied a Gaussian low-pass filter to the V_{res} images in Fourier space with a cutoff frequency equivalent to a spatial distance of $\approx 500 \text{ pc}$ to highlight relevant and large perturbations (see Appendix D.1). This allows us to smooth out local and discrete perturbations, and focus on large-scale and coherent features. Based on these images, using a circular grid centered at the center of the galaxy, evenly spaced by $0.3 R_{\text{opt}}$, as shown in Figure 3, we select as potential candidates all those galaxies where the perturbations cover at least an azimuthal extension of 60° . We consider perturbations that at a given azimuthal angle cover a radial extension $\lesssim 0.3 R_{\text{opt}}$ as corrugation patterns, whereas the remaining as typical warps.

Examples of the resulting filtered images are shown in Figure 3. The upper panel shows an example of well-defined global and coherent velocity perturbations. The bottom panel shows the case where the map was consistent with an unperturbed velocity field. According to these criteria, eight galaxies show V_{res} maps consistent with a vertical perturbed disk.

We note that previous studies have analyzed velocity dispersion maps, V_{disp} , to identify vertically perturbed disk galaxies. For example, Jiménez-Vicente & Battaner (2000) used V_{disp} to detect plausible shells or chimneys in the galactic disk of NGC 5668. This was done by comparing the geometry of the V_{res} and V_{disp} maps and associating local perturbations in both maps to vertical motions in the galaxy. In our work, V_{disp} maps are obtained as a subproduct of the data reduction process (see Section 3), and thus, we present them together with the V_{res} maps. However, as opposed to Jiménez-Vicente & Battaner (2000), our goal here is to identify global rather than localized and discrete velocity perturbations. As a result, V_{disp} maps were not explored in detail. We will further analyze these maps in follow-up work.

We emphasize that our selection criteria cannot confirm or rule out the presence of vertical perturbations in our disks. Although the objective is to detect global and coherent perturbations, it should be noted that our method does not exclude the presence of fountain flows, which are shown as local and discrete perturbations, but rather, both types of perturbations could coexist. Nonetheless, note that we have carefully checked the H_α intensity profiles in all galaxies that were selected as potential vertically perturbed objects. We found that all candidates within the WiNDS sample show, in general, well-behaved Gaussian profiles. That is, there is no presence of strong and intense multiple components in the H_α profiles due to the presence of other velocity components (such as those observed in merging systems such as HCG 31, for example, Amram et al. 2007).

6. Results

In this section, we analyze and discuss the resulting V_{res} fields of the eight WiNDS galaxies that fulfilled our quantification criteria described in Section 5. However, we discuss the remaining newly observed galaxies in Appendix A.1 and in Appendix B.1 we present the V_{res} maps of galaxies that do not accomplish the criteria described in Section 5.

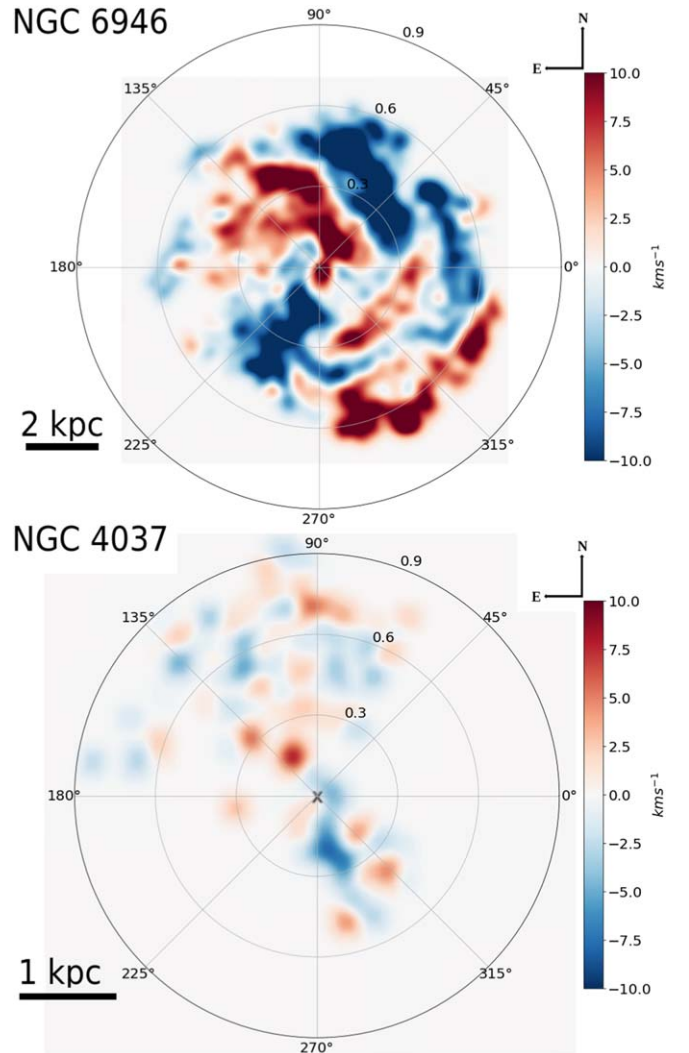


Figure 3. Filtered V_{res} images. Top panel: NGC 6946 galaxy with well-defined velocity perturbations covering azimuthal extensions $>60^\circ$ and radial extension $\lesssim 0.3 R_{\text{opt}}$ at a given azimuthal radius. Bottom panel: NGC 4037 galaxy without signs of global perturbation. The contours represent $0.3 R_{\text{opt}}$ for each galaxy.

In Figure 4, we show the results obtained for the galaxy NGC 3344. This galaxy has a very low morphological inclination angle ($i \sim 18^\circ$, Paturel et al. 1997), and thus, represents an ideal candidate to search for vertical perturbations on its galactic disk. In panel (a) we show a B -band image of the galaxy, obtained from the XDSS (see footnote 3). The galaxy shows a well-defined flocculent spiral structure and a weak bar inside the inner ring (Verdes-Montenegro et al. 2000). It has an optical radius, R_{opt} , of 7.7 kpc (RC3; de Vaucouleurs et al. 1991), i.e., approximately half the size of the Milky Way. In panel (b) we show the resulting V_{los} map, obtained following the procedure outlined in Section 3. The map shows good H_α coverage of the overall disk ($1 R_{\text{opt}}$), despite being limited by the FoV of the GHASP instrument. The amplitude of V_{los} reaches $\approx 100 \text{ km s}^{-1}$. Panel (c) shows the H_α velocity dispersion map, normalized to $\sigma_{95\text{th}} = 44.2 \text{ km s}^{-1}$ ¹³

¹³ A normalization of the velocity dispersion to the 95th percentile was used for all galaxies in order to avoid outlying dispersion measurements and better show possible correlations between the residual velocity fields and velocity dispersion.

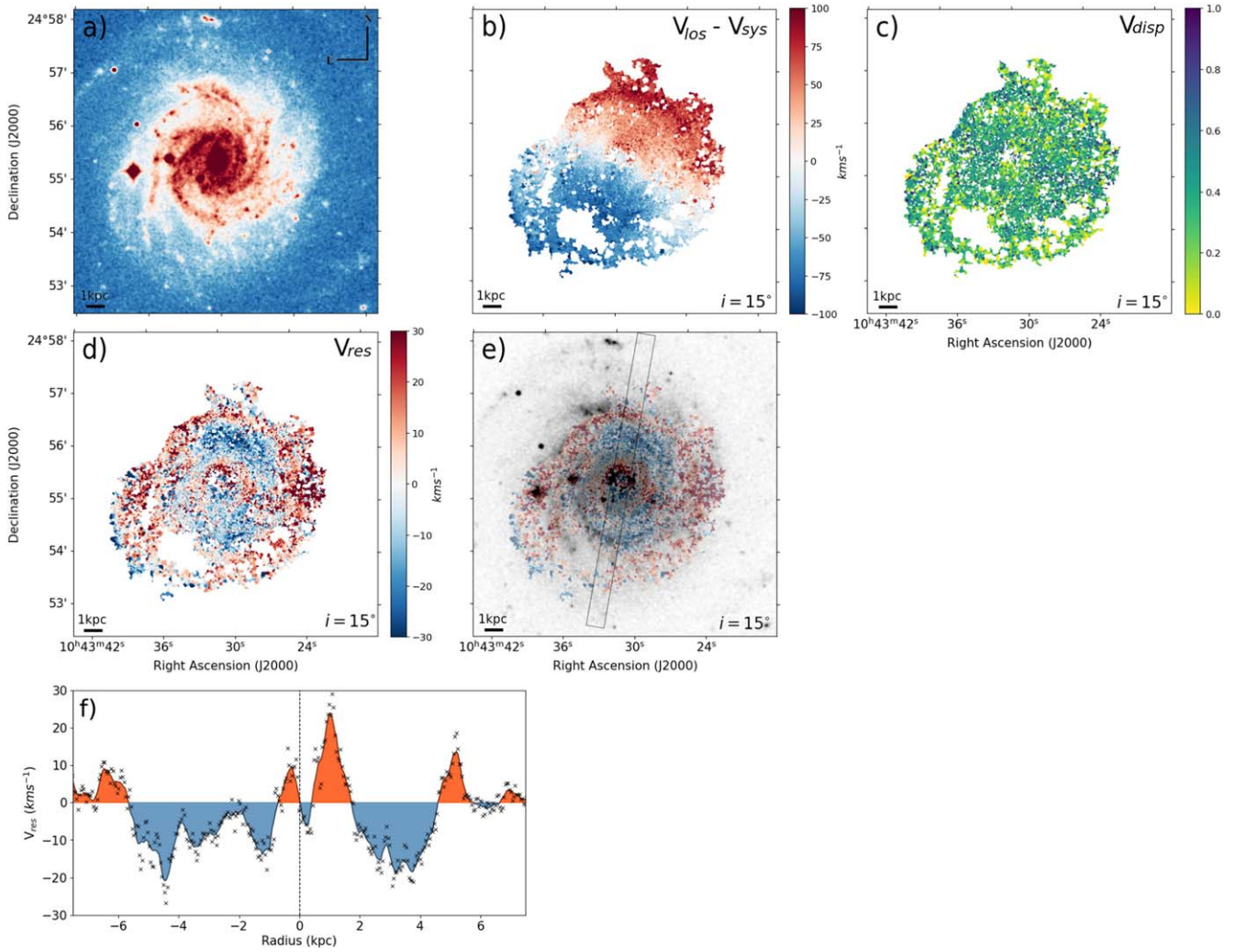


Figure 4. NGC 3344. Panel (a): XDFSS blue-band image. Panel (b): H_{α} velocity field. Panel (c): H_{α} velocity dispersion map normalized to 44.2 km s^{-1} corresponding to the 95th percentile corrected for instrumental broadening. Panel (d): H_{α} residual velocity field. Panel (e): optical band image with the H_{α} residual velocity field. Panel (f): residual velocity radial profile considering a slit indicated by black lines with a PA of 10° in panel (e). The black line corresponds to the smoothed curve and the dashed line fits the center of the galaxy indicated in panel (e). The red (blue) area corresponds to velocities above (below) the midplane of the galaxy. The derived kinematic inclination is indicated in the lower right of each panel.

Panel (d) shows the residual velocity field, V_{res} , obtained after subtracting the axisymmetric rotational velocity model from V_{los} . Interestingly, the V_{res} map reveals a global, strong, and coherent oscillating-like pattern throughout the entire disk of the galaxy, with an amplitude of the order of $\pm 30 \text{ km s}^{-1}$. To compare the disk morphology to the structure observed on its residual velocity field, in panel (e) we show the galaxy B -band image with the contours obtained from the V_{res} field. Notice that no clear correlation between axisymmetric patterns and velocity perturbations can be observed. The extended black box or slit, placed across the disk in panel (e), highlights the multiple transitions from positive to negative values experienced by V_{res} as a function of galactocentric distance. This is better shown in panel (f) where we highlight the behavior of V_{res} across this particular slit (black crosses). Here, the black line represents the corresponding smoothed data using a moving average function with a seven data point window, while the dashed vertical line indicates the galaxy center. The direction of the slit was chosen to highlight transitions of the residual velocity values. NGC 3344 is a galaxy that is cataloged as isolated, with no nearby galaxies within a projected radial

distance of 150 kpc and radial velocity difference $\Delta \leq 500 \text{ km s}^{-1}$. We recall that NGC 3344 has a very mildly inclined disk, $i \sim 18^{\circ}$. Thus, the contribution from in-plane flows to the resulting V_{res} , associated with, e.g., bars and/or spiral structure, is expected to be small. As previously discussed, a plausible interpretation of these V_{res} perturbations is associated with the contribution from a vertical corrugation pattern. Such corrugation pattern could be the result of several mechanisms, such as close interactions with satellites (Jiang & Binney 1999; Sancisi et al. 2008; Roškar et al. 2010; Aumer et al. 2013; Radburn-Smith et al. 2014; Gómez et al. 2017), torques associated with either misaligned triaxial DM halos or even DM overdensity wakes (Ostriker & Binney 1989; Quinn et al. 1993; Velazquez & White 1999; Bailin 2003; Kazantzidis et al. 2009; Gómez et al. 2013; D’Onghia et al. 2016). Vertical perturbations on this galaxy have previously been reported by other authors. Indeed, Briggs (1990) reports the presence of a warp in the outer regions of NGC 3344 after analyzing observations of the HI 21 cm line. Verdes-Montenegro et al. (2000) presented a detailed study of this galaxy, also using HI 21 cm lines. The authors suggest a possible relationship

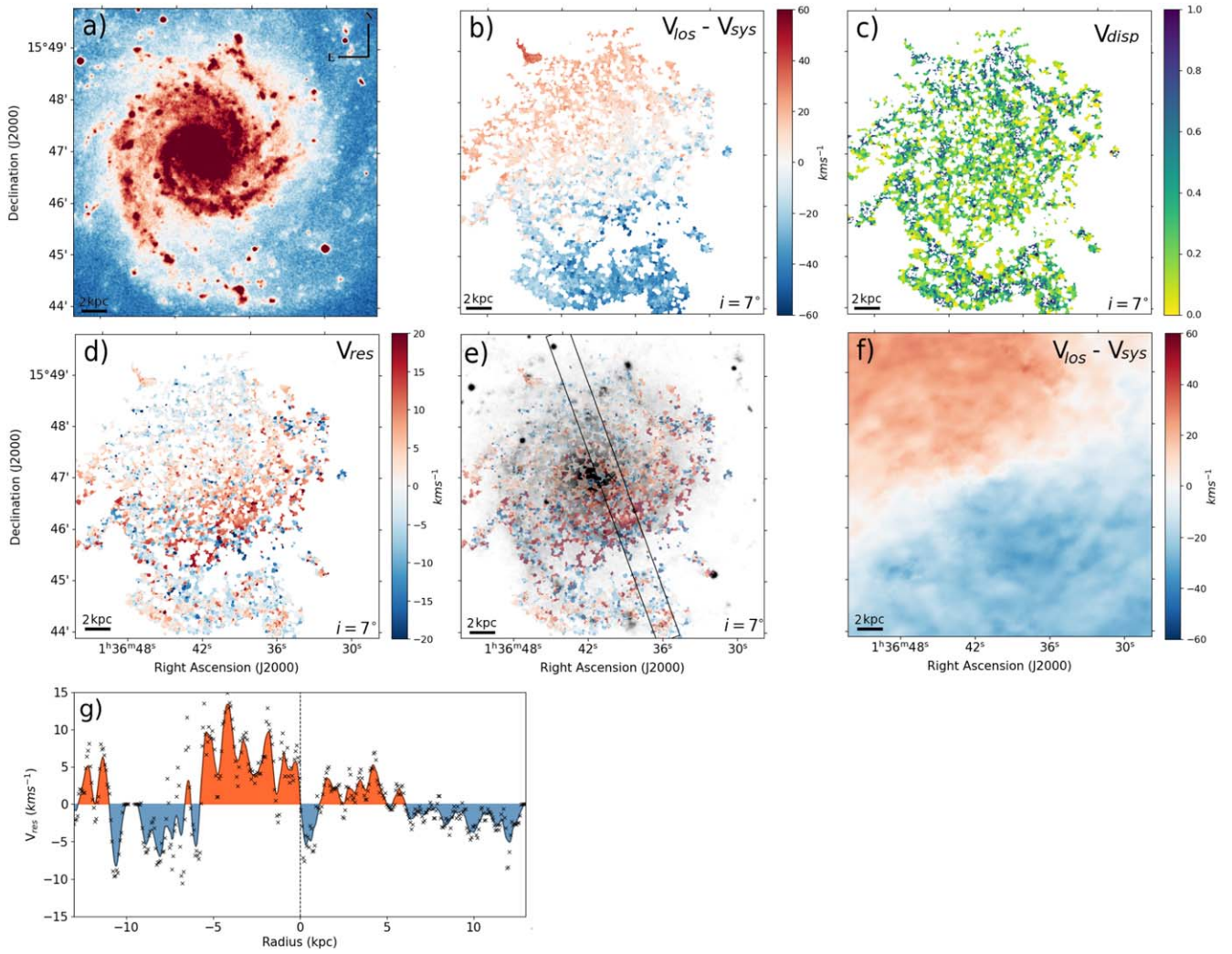


Figure 5. NGC 628. Panel (a): XDFSS blue-band image. Panel (b): H_{α} velocity field. Panel (c): H_{α} velocity dispersion map normalized to 14 km s^{-1} corresponding to the 95th percentile. Panel (d): H_{α} residual velocity field. Panel (e): optical band image with the H_{α} residual velocity field. Panel (f): HI H I velocity field from the THINGS survey Walter et al. (2008). Panel (g): residual velocity radial profile considering a slit indicated by black lines with a PA of 160° in panel (e). The black line corresponds to the smoothed curve and the dashed line fits the center of the galaxy indicated in panel (e). The red (blue) area corresponds to velocities above (below) the midplane of the galaxy. The derived kinematic inclination is indicated in the lower right of each panel.

between the inner and outer star-forming rings with a strong spiral structure and the warp in the HI layer. However, they were not able to clearly link the warp structure with the perturbation in the more internal regions. Our analysis of NGC 3344, with a spectral resolution $\sim 10 \text{ km s}^{-1}$, reveals a very complex structure of NGC 3344. NGC 3344 is a very interesting candidate of the vertically perturbed galaxy that will be analyzed in greater detail in a follow-up study.

In Figure 5, we now show the results obtained for NGC 628 (M74). This is a nearly face-on galaxy with an inclination angle of 6.5° , and thus, an ideal candidate to search for possible vertical perturbations. In panel (a), we display a B -band image of the galaxy, obtained from XDFSS. NGC 628 is a non-barred galaxy with two main spiral arms emerging from its bulge. The H_{α} observation coverage of NGC 628 corresponds to a mean radius of 12.5 kpc, which represents $0.8 R_{\text{opt}}$. The H_{α} velocity map (panel (b)) shows an amplitude of $\sim 60 \text{ km s}^{-1}$, as expected from a low-inclination galaxy. For comparison, we also show in panel (f) the HI velocity map from The HI Nearby Galaxy Survey (THINGS; Walter et al. 2008) observed with the Very Large Array (VLA), which is consistent with the H_{α} velocity map. Interestingly, studies

based on neutral hydrogen (Kamphuis & Briggs 1992) have detected the presence of an elongated warp structure at around a $12'$ projected distance from the nucleus. In panel (c), we show the derived H_{α} velocity dispersion map, normalized to $\sigma_{95\text{th}} = 14 \text{ km s}^{-1}$. The V_{res} field of NGC 628 is shown in panel (d). Interestingly, global and coherent velocity perturbations, of the order of 20 km s^{-1} , can be clearly observed. Panel (e) allows us to correlate NGC 628-disk morphology with its residual velocity map. The velocity perturbations on this galaxy are more clearly highlighted in panel (g) where we follow the mean V_{res} along the highlighted slit, suggesting a warp-like structure.

As shown in its B -band image (panel (a)), an extended tail is observed in the southwest direction of the disk. This substructure has previously been reported in Kamphuis & Briggs (1992). Although NGC 628 currently has no close companions, a dwarf galaxy system (UGC 1176 and UGC 1171) is located at 140 kpc. The overall mass of the satellite system has been reported to lie on the order of magnitude of the total NGC 628 mass (Michalowski et al. 2020). This system may have played an important role in the evolution of NGC 628. As discussed by Briggs (1986), if the dwarf system is at rest at its current location concerning NGC 628,

it would fall into its host in about 1–2 Gyr. However, a more recent study by Michałowski et al. (2020) suggests that a tidal origin for the asymmetric HI I tail located on the southwestern outskirts is an unlikely scenario. They argue that the tail does not resemble recent tidal features, whereas an older feature would wind almost symmetrically around the galaxy. In addition, recently induced tidal tails typically show $m=2$ patterns, with two nearly symmetrical arms. Instead, NGC 628 shows a strong $m=1$ -like spiral structure. Nonetheless, they do not rule out a possible previous interaction with the neighboring dwarf pair. It is interesting to compare with the results presented in Gómez et al. (2017), based on fully cosmological simulations. In particular, their model S13 shows morphology similar to that of NGC 628, with a strong $m=1$ arm extending from the inner galactic regions. This model displays a vertically perturbed stellar and cold gas disk, but no recent interaction with massive satellites ($M_{\text{sat}}/M_{\text{host}} > 0.03$). Instead, S13 experienced a massive gas-rich merger 5 Gyr ago. As a result, its preexisting disk was destroyed but a new thin disk quickly formed thereafter due to the re-accretion of misaligned gas. This gas accretion gives rise to both the vertical perturbations observed in this modeled galaxy and its strong $m=1$ morphology. This suggests that the velocity perturbations observed in NGC 628, as well as its $m=1$ spiral morphology, could be linked to the recent accretion of misaligned cold gas.

In Figure 6, we focus on NGC 6946. This is a spiral galaxy classified as SABcd with a kinematical inclination of $i \sim 17^\circ$, an optical radius of ≈ 10 kpc, and an estimated total mass of $1.2 \times 10^{11} M_\odot$ (Pisano & Wilcots 2000). Optical and neutral hydrogen observations of NGC 6946 have revealed its strong spiral arms, a particularly high star formation rate, a nuclear starburst, and a weak bar (Pisano & Wilcots 2000; Schinnerer et al. 2006). Panel (a) shows its XDSS B -band image, where we can clearly see its spiral nature. NGC 6946 is considered to be isolated (Tully 1988). Using HI observations, previous studies have detected a dozen low mass irregular dwarf galaxies companions (Karachentsev et al. 2000; Pisano & Wilcots 2000; Karachentsev et al. 2005). However, at the present day, NGC 6946 does not show any signs of undergoing strong direct gravitational interactions with its satellite population. Its two most massive companions, UGC 11583 and L149, have estimated total masses of 1.5×10^9 and $3.0 \times 10^8 M_\odot$ and projected distances of 83 and 75 kpc, respectively (Pisano & Wilcots 2000). The H_α V_{los} map of NGC 6946, shown in panel (b), has an amplitude of $\sim 150 \text{ km s}^{-1}$. Following our selection criteria, the map reveals significant H_α coverage, reaching at least a radius of 7 kpc, corresponding to $0.7 R_{\text{opt}}$. As in the case of NGC 3344, the coverage for NGC 6946 is limited by the FoV of the GHASP instrument. For comparison, we show (in panel (f)) the HI velocity map extracted from Walter et al. (2008). Both maps are consistent, even though they consider different components of the interstellar medium (ISM) and come from different instruments and techniques. Note, however, that our observations have a better spatial resolution of $3''$ against the $6''$ – $12''$ resolution in the observations. The H_α velocity dispersion map is shown in panel (c), normalized to $\sigma_{95\text{th}} = 55.2 \text{ km s}^{-1}$. In panels (d) and (e), we show the galaxy V_{res} map, which reveals global and coherent perturbations, reaching amplitudes $\lesssim 35 \text{ km s}^{-1}$. The V_{res} velocity contours, overlaid on the B -band image (panel (e)), allow us to directly contrast this velocity structure with the morphology of NGC 6946. The oscillating nature of this velocity field is better highlighted in panel (g), where we show the mean V_{res} along the highlighted slit in panel (e). It is worth recalling the spiral nature of NGC 6946, and its low but not negligible inclination. As a result, a

contribution from in-plane flow to the V_{res} field can be expected. However, as shown by Gómez et al. (2021), for disks as inclined as NGC 6946 ($i \sim 40^\circ$), even a spiral structure 1000 times denser than its mean background disk density cannot generate velocity perturbations with amplitudes $\gtrsim 10 \text{ km s}^{-1}$. This indicates that the observed global velocity perturbation could be partially linked to vertical velocity flows.

It is interesting to consider what mechanisms could be driving the perturbations in this galaxy. As previously discussed, NGC 6946 does not have nearby massive satellites that could be directly tidally interacting with its disk. However, even low mass satellites at relatively large galactocentric distances could significantly perturb an embedded disk through the excitation of dark matter overdensity wakes (Weinberg 1998; Vesperini & Weinberg 2000). For example, using cosmological simulations of Milky Way-mass galaxies, Gómez et al. (2016) studied the onset and evolution of a strong vertical pattern in the disk. The vertical pattern in this model, with an amplitude of $\sim 50 \text{ km s}^{-1}$, is the result of a satellite-host halo-disk interaction. Interestingly, the satellite had a total mass of $\sim 5\%$ of the host and a pericenter distance of 80 kpc. The satellite was not massive enough to directly perturb the galactic disk but the density field of the host dark matter halo responded to the satellite passage and strongly amplified its perturbative effects. A similar scenario could be taking place in the case of NGC 6946, considering its low mass companions at a relatively large projected galactocentric distance. Other possible mechanisms, in addition to the previously discussed contribution from in-plane flows, could be related to the smooth accretion of misaligned cold gas.

In Figure 7, we show NGC 4321 (M100), a grand-design nearby spiral galaxy belonging to the Virgo Cluster, classified as SABbc (RC3). The galaxy has a small bulge and two well-defined, prominent, and symmetric spiral arms, as shown in its B -band image (panel (a)). The nucleus of the galaxy is compact and bright. NGC 4321 is a very low-inclination galaxy, with a kinematical inclination of $i \approx 25^\circ$ and an optical radius of $R_{\text{opt}} = 16.3$ kpc from RC3. Panel (b) shows that the coverage of the V_{los} distribution, obtained from the H_α observations, is extensive and nearly reaches nearly its optical radius, i.e., $13 \text{ kpc} \sim 0.8 R_{\text{opt}}$. The V_{los} map shows an amplitude of $\approx 150 \text{ km s}^{-1}$. For completeness, we show in panel (c) the H_α velocity dispersion map, normalized to $\sigma_{95\text{th}} = 33.1 \text{ km s}^{-1}$.

The derived residual velocity map, obtained after subtracting the axisymmetric velocity model is shown in panels (d) and (e). As in previous examples, this map reveals global and coherent velocity flows with amplitudes that can reach $\sim 30 \text{ km s}^{-1}$. Panel (f) more clearly shows the radial variations of the residual velocity along the highlighted slit in panel (e). Note the oscillatory behavior of V_{res} across the disk. These perturbations, observed in the ionized gas of NGC 4321, could be the result of a recent interaction with one of its satellite galaxies. Indeed, NGC 4321 has two dwarf companion galaxies, NGC 4328 and NGC 4323, located at projected distances of 24 and 28 kpc from their host, respectively (Hernandez et al. 2005). Knapen et al. (1993) showed that the HI component of NGC 4321 is mostly contained within the optical disk. However, they also identify a large HI extension that could be the result of the tidal interaction with NGC 4323. Indeed, Knapen et al. (1993) find important differences in the behavior of its rotation between the approaching and the receding sides. They suggest these differences could be caused by deviations from circular motions in the outer disk probably due to a close passage of its companion galaxy. They also suggest this interaction could be the cause of the observed asymmetry in the total HI distribution.

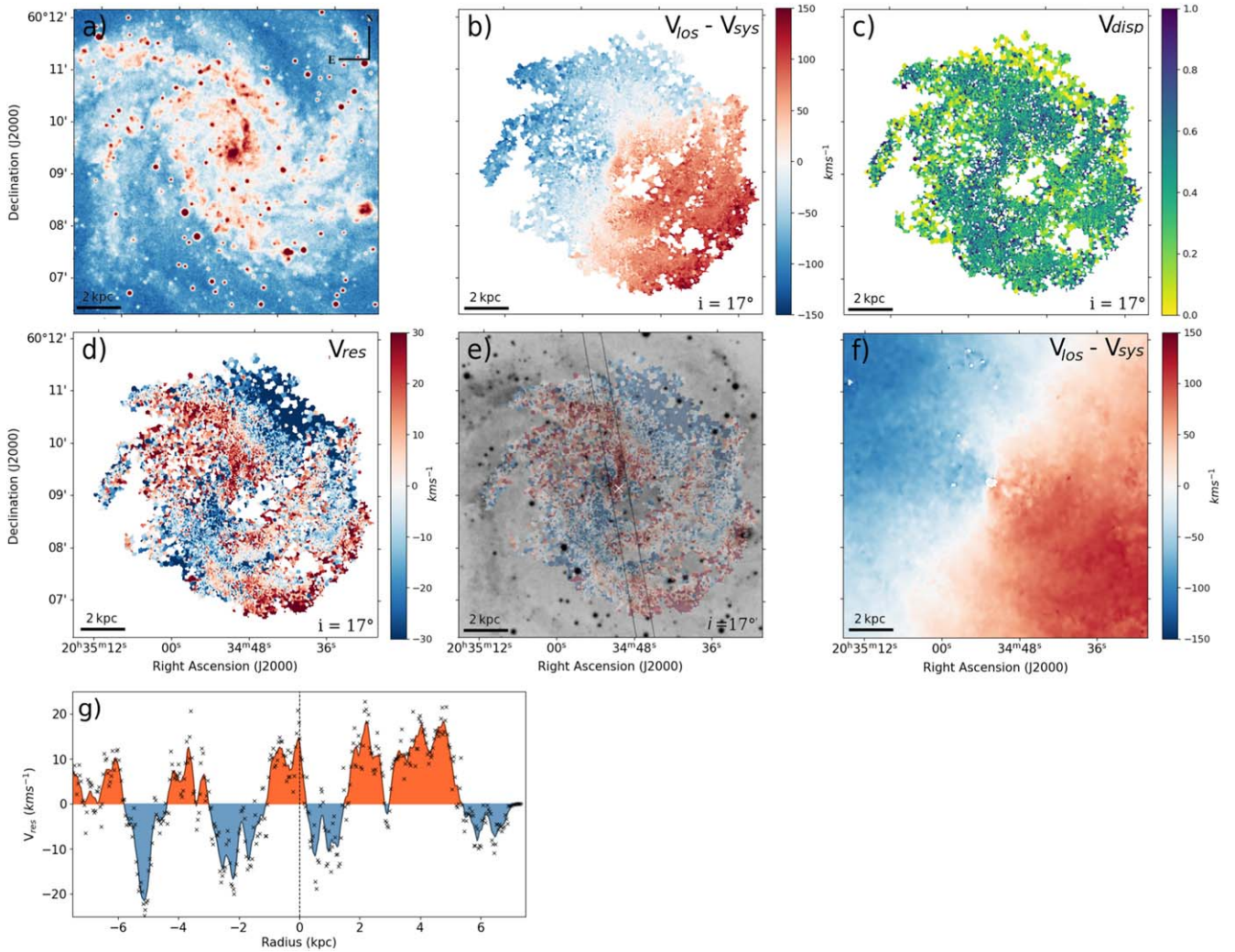


Figure 6. NGC 6946. Panel (a): XDFSS blue-band image. Panel (b): H_{α} velocity field. Panel (c): H_{α} velocity dispersion map normalized to 55.1 km s^{-1} corresponding to the 95th percentile. Panel (d): H_{α} residual velocity field. Panel (e): optical band image with the H_{α} residual velocity field. Panel (f): HI velocity field from the THINGS survey Walter et al. (2008). Panel (g): residual velocity radial profile considering a slit indicated by black lines with a PA of 170° in panel (e). The black line corresponds to the smoothed curve and the dashed line fits the center of the galaxy indicated in panel (e). The red (blue) area corresponds to velocities above (below) the midplane of the galaxy. The derived kinematic inclination is indicated in the lower right of each panel.

NGC 4321 also shows diffuse stellar extension in two directions, one of them toward NGC 4323, likely the result of ongoing interaction with this satellite (Hernandez et al. 2005).

NGC 5194 (M51a) is a well-known nearby grand-design spiral galaxy classified as non-barred by RC3, with a very low-inclination angle $i = 20^{\circ}$. NGC 5194 is tidally interacting with its companion NGC 5195 (M51b), an early-type SB0 galaxy. NGC 5194 shows an intense star formation activity at its center and along its spiral arms. Panel (a) in Figure 8 clearly shows its strong spiral structure with signs of being lopsided, likely due to the interaction with its companion. Panel (b) shows that the H_{α} observations provide wide coverage of the disk, which allows us to obtain its velocity field up to distances of $12 \text{ kpc} \sim 0.8 R_{\text{opt}}$. The resulting V_{los} map shows a velocity range of $\approx 150 \text{ km s}^{-1}$. It is interesting to compare our H_{α} velocity map with the one derived from HI observations, obtained from THINGS using VLA (Walter et al. 2008), shown in panel (f). As seen in NGC 628 and NGC 6946, the HI velocity map of NGC 5194, constrained to the same FoV as the H_{α} data, shows a very good agreement with the ionized gas velocity map, despite differences

in both the spatial and spectral resolutions. In panel (c), we show the velocity dispersion map normalized to $\sigma_{95\text{th}} = 15 \text{ km s}^{-1}$.

The residual velocity map is shown in panels (d) and (e). It is interesting to note the large velocity perturbations throughout the disk, reaching amplitudes of 40 km s^{-1} . We recall the very low-inclination angle of this galaxy, thus rendering it unlikely that these velocity perturbations are mainly due to in-plane velocity flow. Panel (e) allows comparing the substructure of the V_{res} map with the galaxy morphology as seen in the B -band image. In panel (g), we follow the smoothed residual velocity profile along the highlighted slit. As before, this allows appreciating the radial oscillatory behavior of V_{res} , consistent with what is expected for a corrugated disk. Shetty et al. (2007) presented a deep kinematic study of NGC 5194 using full 2D velocity distributions from interferometric CO and FP H_{α} observations. They report a complex velocity field, with variations of the disk's PA and inclination along the galactic radius that strongly suggest a vertically perturbed disk and very significant out-of-plane motions. An HIHI warp has also been previously reported in NGC 5194 (Rots et al. 1990; Haan & Braun 2014; Oikawa & Sofue 2014), which has been attributed to the tidal interaction with NGC 5195.

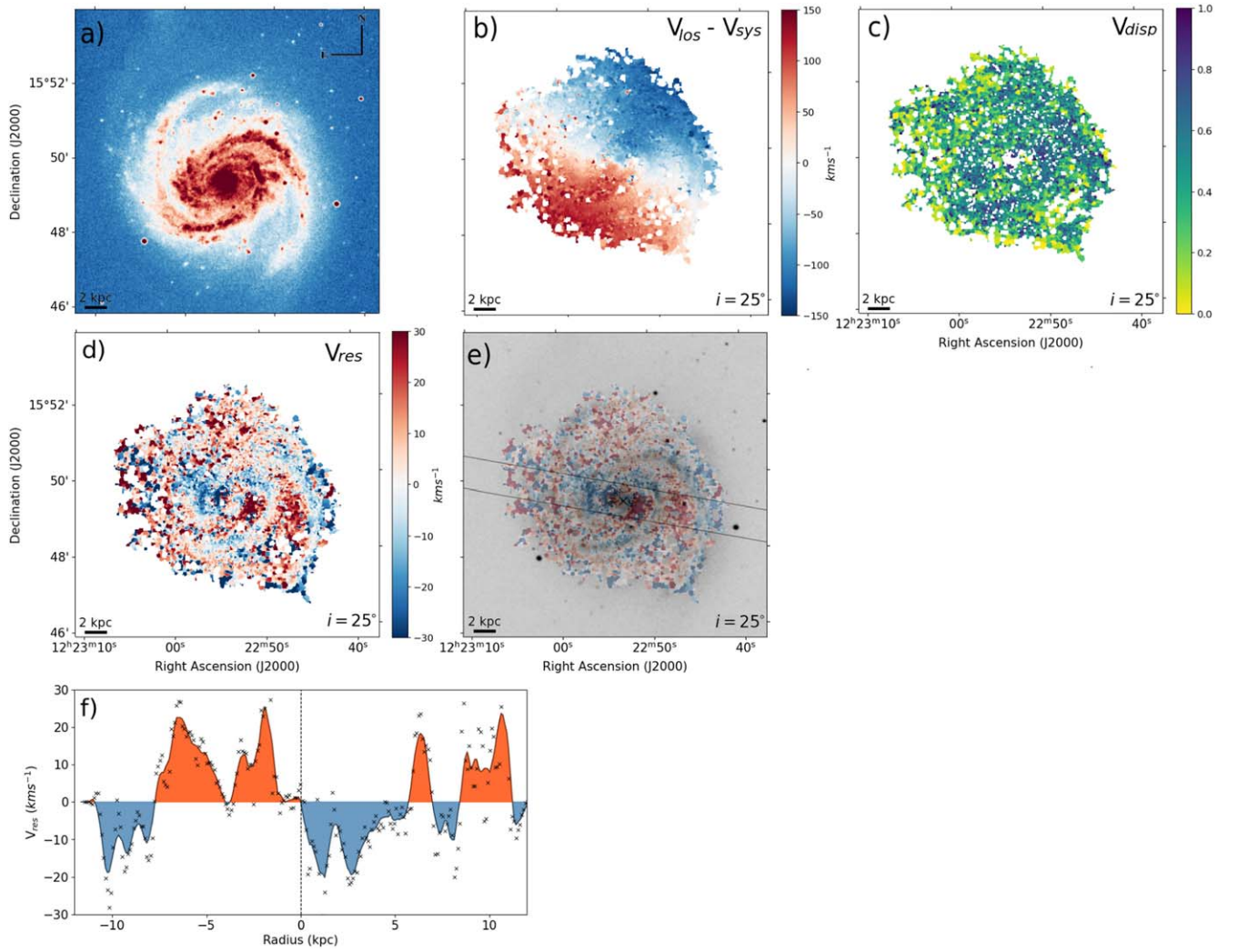


Figure 7. NGC 4321. Panel (a): XDFSS blue-band image. Panel (b): $H\alpha$ velocity field. Panel (c): $H\alpha$ velocity dispersion map normalized to 33.1 km s^{-1} corresponding to the 95th percentile. Panel (d): $H\alpha$ residual velocity field. Panel (e): optical band image with the $H\alpha$ residual velocity field. Panel (f): residual velocity radial profile considering a slit indicated by black lines with a PA of 100° in panel (e). The black line corresponds to the smoothed curve and the dashed line fits the center of the galaxy indicated in panel (e). The red (blue) area corresponds to velocities above (below) the midplane of the galaxy. The derived kinematic inclination is indicated in the lower right of each panel.

The presence of vertical velocity flows in this very interesting galaxy will be further analyzed in a follow-up study, following the procedure described in Gómez et al. (2021).

In Figure 9, we present NGC 5668, a nearly face-on late-type spiral galaxy with an estimated inclination angle of 18° (Schulman et al. 1996) and R_{opt} of $\sim 14.3 \text{ kpc}$, located at 27.6 Mpc . The galaxy is classified as a SA(s)d by RC3, and on its optical image (panel a), it shows a weak bar or oval structure in its inner $12''$ region. Observations of NGC 5668 were extracted from the GHASP sample (Epinat et al. 2008b). The $H\alpha$ coverage reaches out to 20 kpc corresponding to $\sim 1.4 R_{\text{opt}}$. In panel (b), we show the resulting V_{los} field, with a velocity amplitude reaching $\approx 70 \text{ km s}^{-1}$. The velocity dispersion map, normalized to $\sigma_{95\text{th}} = 57.5 \text{ km s}^{-1}$, is shown in panel (c).

The V_{res} map, shown in panel (d), reveals global perturbations with amplitudes $> 20 \text{ km s}^{-1}$, which are also consistent with a warped $H\alpha$ disk. In panel (e), we present the optical image with the overlay of the residual velocity map. The warp is better shown in panel (f), where we can see the mean velocity profile along the highlighted slit in panel (e). Note the large amplitude of this kinematical perturbation

reaching velocities $> 20 \text{ km s}^{-1}$ at the disk outskirts. High-resolution observations in the 21 cm line of the neutral hydrogen velocity field, from VLA, have detected a kinematic warp that begins, at least, at the end of the optical radius (Schulman et al. 1996). Note that the $H\alpha$ warp is very well aligned with the previously reported HI warp, indicating that the perturbation extends even within the optical radius of the galaxy. In addition to the HI kinematic warp, Schulman et al. (1996) detected high-velocity wings beyond the double-horned 21 cm profile, related to high-velocity clouds (HVCs) in the disk and halo of the galaxy. As discussed by Schulman et al. (1996), the high-velocity wings located outside the optical disk may be the result of infalling material, comparable to the Magellanic Stream observed in the Milky Way.

The origin of the kinematic warp, and the infalling material, could be related to a past interaction with its neighbor galaxy UGC 9380, currently located at a projected distance of $\sim 200 \text{ kpc}$ of NGC 5668. It is worth mentioning that Jiménez-Vicente & Battaner (2000) also analyzed the 2D velocity field of this galaxy through its $H\alpha$ emission using an FP interferometer. However, they did not cover the region

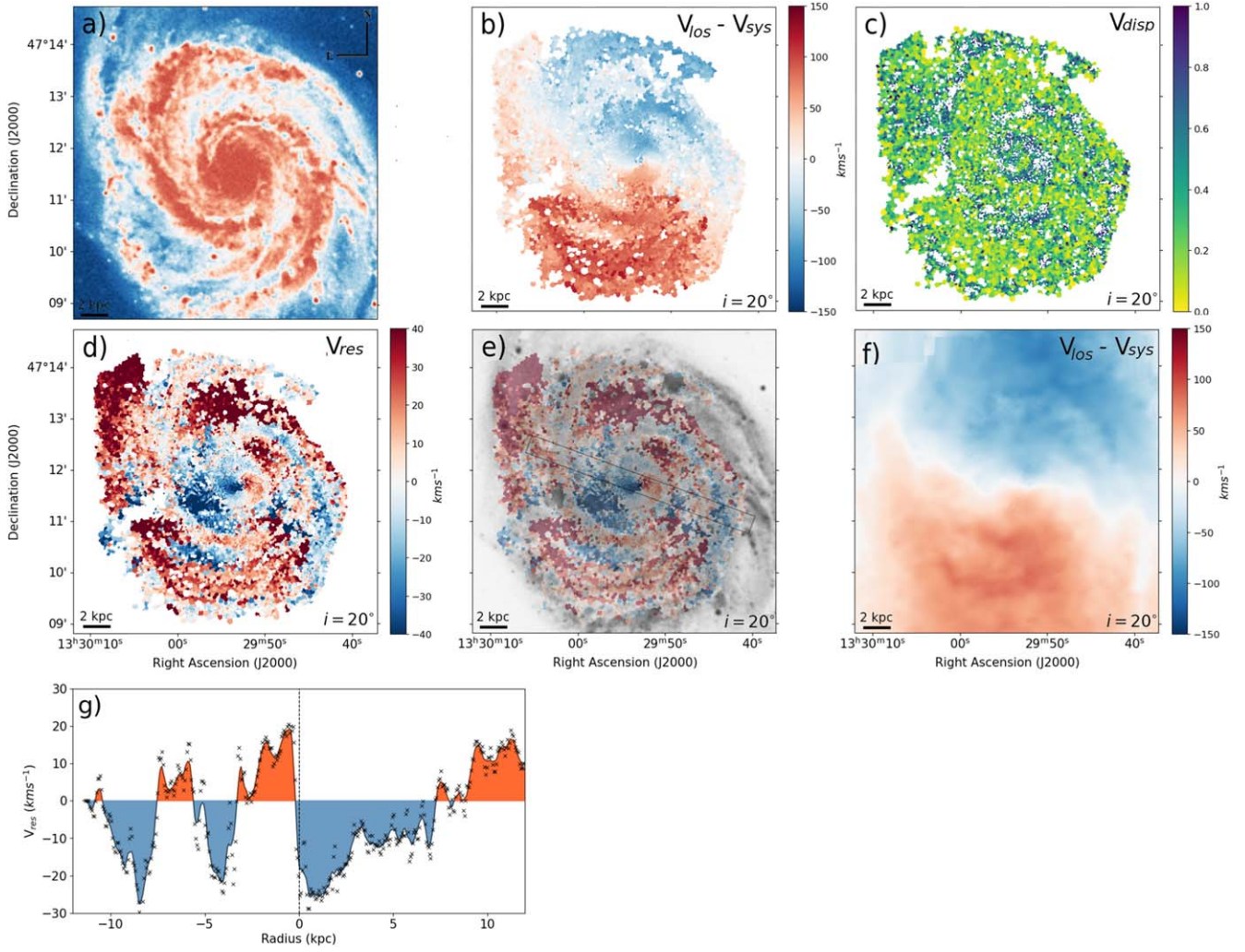


Figure 8. NGC 5194. Panel (a): XDFSS blue-band image. Panel (b): H_{α} velocity field. Panel (c): H_{α} velocity dispersion map normalized to 15 km s^{-1} corresponding to the 95th percentile. Panel (d): H_{α} residual velocity field. Panel (e): optical band image with the H_{α} residual velocity field. Panel (f): HI velocity field from the THINGS survey (Walter et al. 2008). Panel (g): residual velocity radial profile considering a slit indicated by black lines with a PA of 110° in panel (e). The black line corresponds to the smoothed curve and the dashed line fits the center of the galaxy indicated in panel (e). The red (blue) area corresponds to velocities above (below) the midplane of the galaxy. The derived kinematic inclination is indicated in the lower right of each panel.

where we detect the kinematic warp. Instead, they reported the detection of HVCs and localized high residual velocity dispersion regions, associating them with shell/chimney regions. Even though we present a velocity dispersion map in panel (c), in this work we have not attempted to recover these regions, typically associated with vertical motions of ionized gas due to star-forming processes.

In Figure 10, we show NGC 2763. This low-inclination disk galaxy ($i \approx 29.5^{\circ}$) is the only object in WINDS observed in the Southern Hemisphere, and one of the first galaxies observed with the SAM-FP instrument (Mendes de Oliveira et al. 2017). The B -band image in panel (a) reveals two main spiral arms, each with multiple sub-arms and a small bar. In addition, it shows a significantly lopsided structure. The galaxy shows an extended H_{α} emission across the disk, reaching up to $0.9 R_{\text{opt}}$, with $R_{\text{opt}} \approx 9.9 \text{ kpc}$. Panel (b) shows its V_{los} maps, with an amplitude of $\approx 100 \text{ km s}^{-1}$. The velocity dispersion map, normalized to $\sigma_{95\text{th}} = 37.2 \text{ km s}^{-1}$, is shown in panel (c).

The resulting V_{res} maps, shown in panel (d), reveal a very complex structure with global residual velocity flows reaching amplitudes $\gtrsim 20 \text{ km s}^{-1}$. In panel (e), we can observe the B -band

image of NGC 2763 with the residual velocity map overlapped, highlighting the region where complex residual velocity perturbations are observed. Interestingly, no detailed kinematical studies of NGC 2763 velocity field, nor companion galaxies within 150 kpc, have been reported. We have confirmed the lack of massive nearby companions by performing a systematic search within a radial projected distance of 250 kpc and radial velocity difference $\Delta \leq 1000 \text{ km s}^{-1}$ using the NASA/IPAC Extragalactic Database. Thus, NGC 2763 is considered an isolated galaxy. As such, it is not clear whether its significantly perturbed morphology and kinematics are the results of a previous minor merger event or due to significantly misaligned smooth gas accretion.

NGC 5713 is oriented nearly face-on, with an inclination $i \approx 10^{\circ}$, and shows a significantly lopsided morphology. This can be seen in panel (a) of Figure 11, where we show its XDFSS B -band image. NGC 5713 has an $R_{\text{opt}} \sim 13.5 \text{ kpc}$, it is a barred and multiple arm spiral galaxy (SABb type; de Vaucouleurs et al. 1991), and is located at 33.4 Mpc. The H_{α} V_{los} map, shown in panel (b), covers a region of $\sim 0.9 R_{\text{opt}}$, and shows an amplitude of $\sim 100 \text{ km s}^{-1}$. The velocity dispersion map, normalized to $\sigma_{95\text{th}} = 54.2 \text{ km s}^{-1}$, is shown in panel (c).

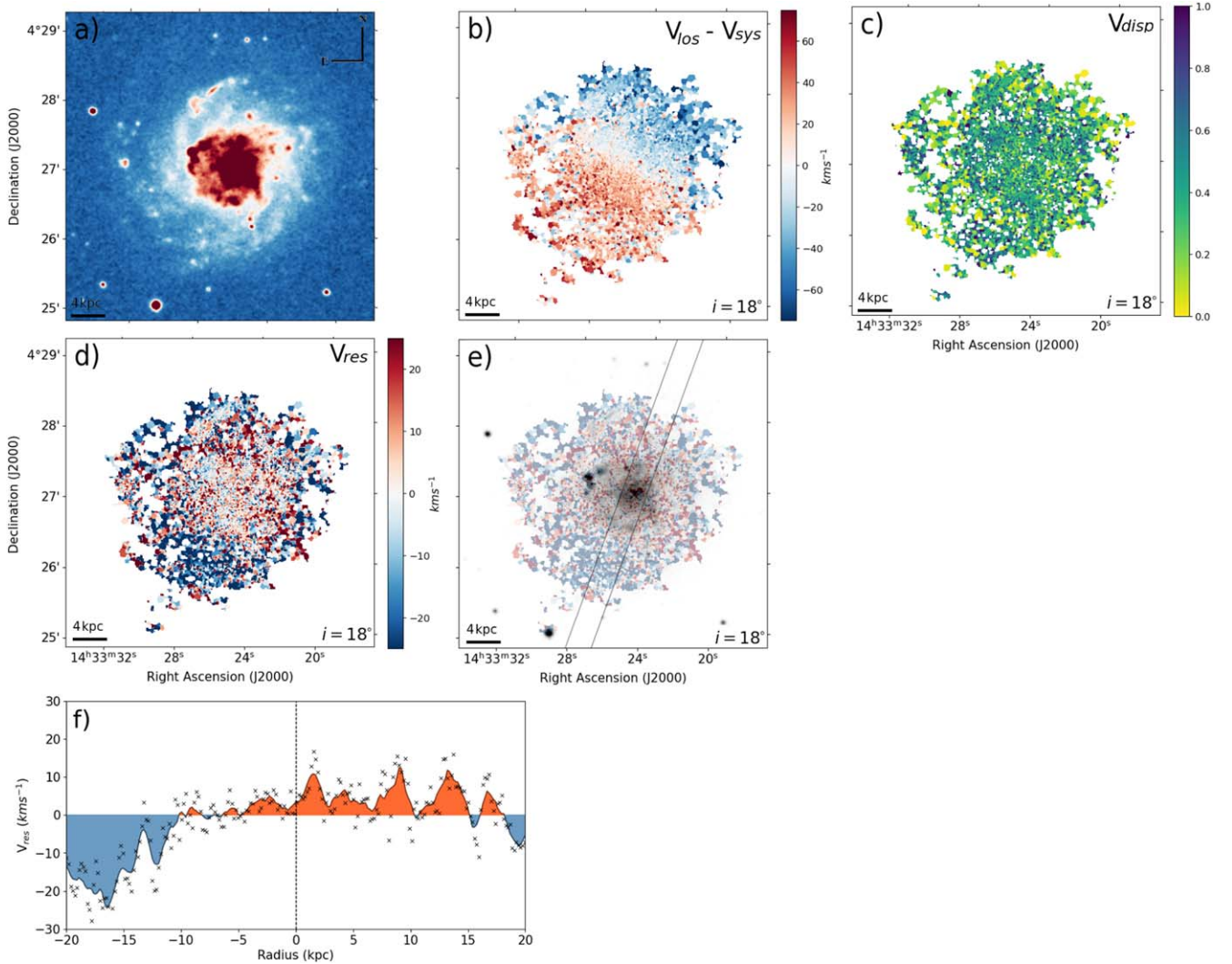


Figure 9. NGC 5668. Panel (a): XDFSS blue-band image. Panel (b): $H\alpha$ velocity field. Panel (c): $H\alpha$ velocity dispersion map normalized to 57.5 km s^{-1} corresponding to the 95th percentile, corrected for instrumental broadening. Panel (d): $H\alpha$ residual velocity field. Panel (e): optical band image with the $H\alpha$ residual velocity field. Panel (f): residual velocity radial profile considering a slit indicated by black lines with a PA of 20° in panel (e). The black line corresponds to the smoothed curve and the dashed line fits the center of the galaxy indicated in panel (e). The red (blue) area corresponds to velocities above (below) the midplane of the galaxy. The derived kinematic inclination is indicated in the lower right of each panel.

The V_{res} (panel (d)) reveals a very peculiar structure, with several global and coherent perturbations reaching peak velocities $\geq 30 \text{ km s}^{-1}$. The galaxy is currently undergoing a very strong tidal interaction with its similar mass Sab-type companion, NGC 5719 (Vergani et al. 2007), and shows two HI tidal tails. Both galaxies (NGC 5713 and NGC 5719) show an optical radius at a similar galactocentric distance and are connected by two HI tidal bridges. The projected distance between these two galaxies is $\sim 77 \text{ kpc}$. NGC 5719 shows an ionized gas disk that counter-rotates with respect to its neutral gas counterpart. According to Vergani et al. (2007), this counter-rotating disk is the result of the accretion of NGC 5713 material onto NGC 5719 during their closest approach. Interestingly NGC 5719 shows a nearly edge-on configuration with a clearly visible warped disk. In addition, NGC 5713 is interacting with the Sm-type dwarf galaxy, PGC 135857, which is located at a projected distance of $\sim 64 \text{ kpc}$ (Vergani et al. 2007). These interactions are likely behind the observed NGC 5713 strongly perturbed velocity field. The interacting system will be compared against numerical models in a follow-up study.

7. Discussion and Conclusions

In this study, we have presented WiNDS, which currently consists of 40 nearby low-inclination spiral galaxies, including objects with diverse morphological features. The WiNDS sample contains galaxies within a distance limit of 45 Mpc and absolute B magnitude between -17.0 and -21.9 mag , all observed in $H\alpha$ with an FP interferometer. These observations allow us to obtain very detailed velocity maps of the ionized gas distribution, with velocity sampling precision as low as 3 km s^{-1} , which translates into a resolution of 6 km s^{-1} . Our sample was selected such that galaxies have an inclination angle $i \lesssim 40^\circ$. WiNDS consists of 12 new data observed, and includes archival data for 28 low-inclination late-type galaxies, extracted from the GHASP, SINGS- $H\alpha$, VIRGO- $H\alpha$, and HRS- $H\alpha$ surveys. For each galaxy in the final sample, we derived their line-of-sight velocity field, an unperturbed axisymmetric velocity model, kinematical parameters, the corresponding residual velocity fields. The results of the reduction are presented in Figures 13–15 and Appendix A.2,

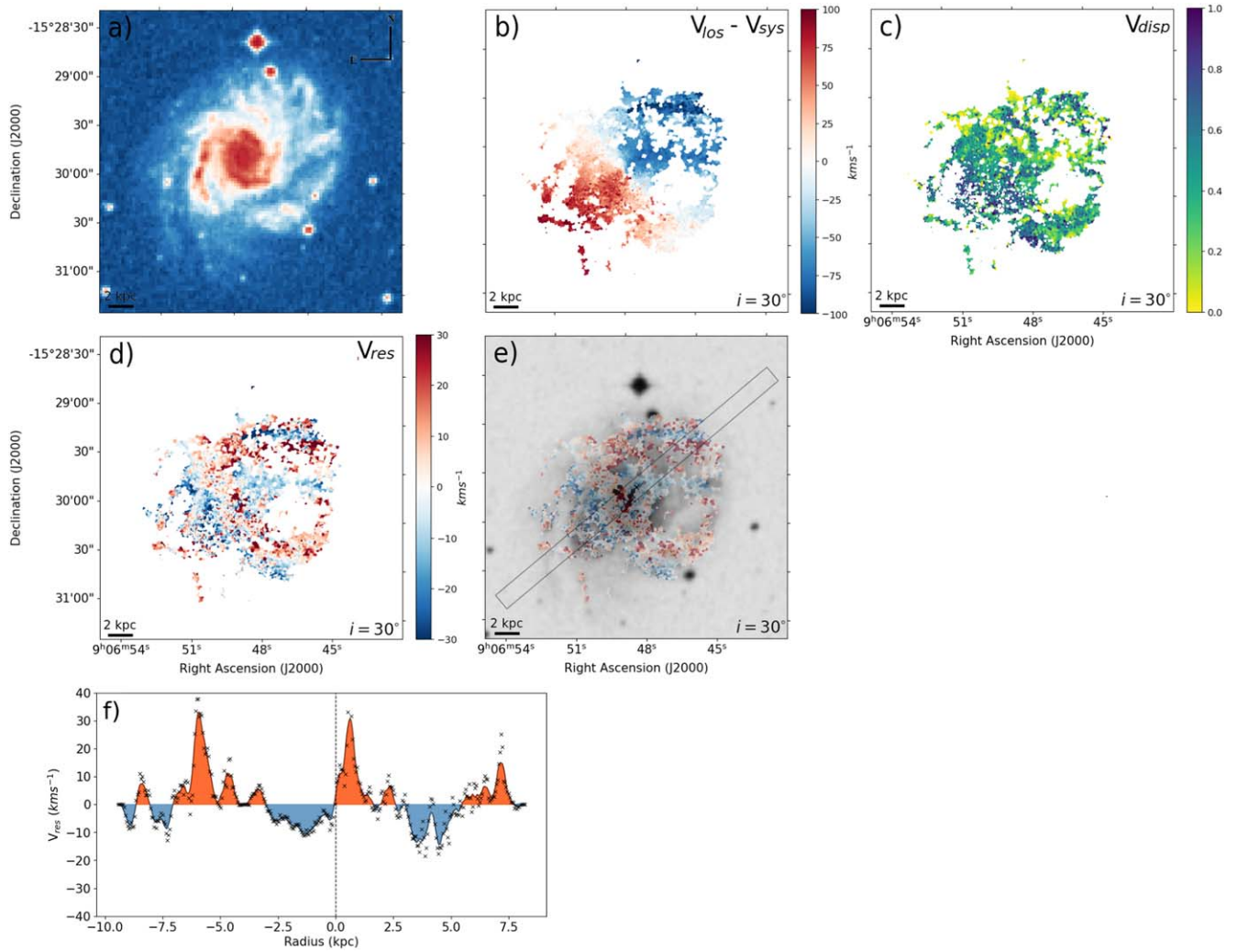


Figure 10. NGC 2763. Panel (a): XDFSS blue-band image. Panel (b): $H\alpha$ velocity field. Panel (c): $H\alpha$ velocity dispersion map normalized to 37.2 km s^{-1} corresponding to the 95th percentile. Panel (d): $H\alpha$ residual velocity field. Panel (e): optical band image with the $H\alpha$ residual velocity field. Panel (f): residual velocity radial profile considering a slit indicated by black lines with a PA of 40° in panel (e). The black line corresponds to the smoothed curve and the dashed line fits the center of the galaxy indicated in panel (e). The red (blue) area corresponds to velocities above (below) the midplane of the galaxy. The derived kinematic inclination is indicated in the lower right of each panel.

A.3 and B.1, respectively. Finally, the rotation curves are displayed in Figure 16 and Appendix C.1.

Our main goal in this work was to examine the resulting V_{res} fields to search for evidence of large, global, and coherent kinematic perturbations in our sample of low-inclination late-type galaxies. In particular, we seek perturbations that are consistent with those produced by warps and corrugation patterns. Through three criteria we identify clear signatures of perturbations. First, we are interested in objects that present a wide $H\alpha$ coverage ($\geq 0.7 R_{\text{opt}}$) so that the kinematics of the disks could be globally explored. Second, we focused on galaxies with V_{res} amplitude that are $> 10 \text{ km s}^{-1}$, which allows us to be more confident in observing perturbations in the low-inclination disks that are not the result of the axisymmetric components of the galaxies. Finally, we also searched for perturbations in the V_{res} fields that show global and coherent velocity flows, avoiding local and discrete perturbations that could be linked to, e.g., fountain flows.

We emphasize that our selection criteria cannot confirm nor rule out the presence of vertical perturbations in our disks. Instead, our goal is to select potentially strong candidates for follow-up studies. Note, however, that as shown by Monari et al. (2016) and

Gómez et al. (2021), the amplitude of the observed velocity flows in these low-inclination disks are, typically, much too large to be driven either by spiral structure or by a bar. Within the subset of galaxies with vertical perturbations considered as candidates, those displaying discrete and local perturbations that could be associated with fountain flows are not excluded since such signatures can coexist with the global and coherent perturbations that we aim at detecting in this study.

A vertical perturbation such as a warp or a corrugation pattern is manifested by an extended and oscillatory vertical displacement of the disk with respect to the overall midplane. Its characterization can allow us to constrain the recent interaction history of a galaxy. Previous studies based on cosmological simulations (e.g., Gómez et al. 2017) have identified four main mechanisms behind such perturbations: distant fly-by massive companions, close satellite encounters, re-accretion of cold gas from progenitors of a gas-rich major merger, and accretion of misaligned cold gas. Out of 40 observed low-inclination galaxies, we find that approximately 20% of the sample shows clear signatures of global and coherent perturbations. Adding to this statistic to the results of

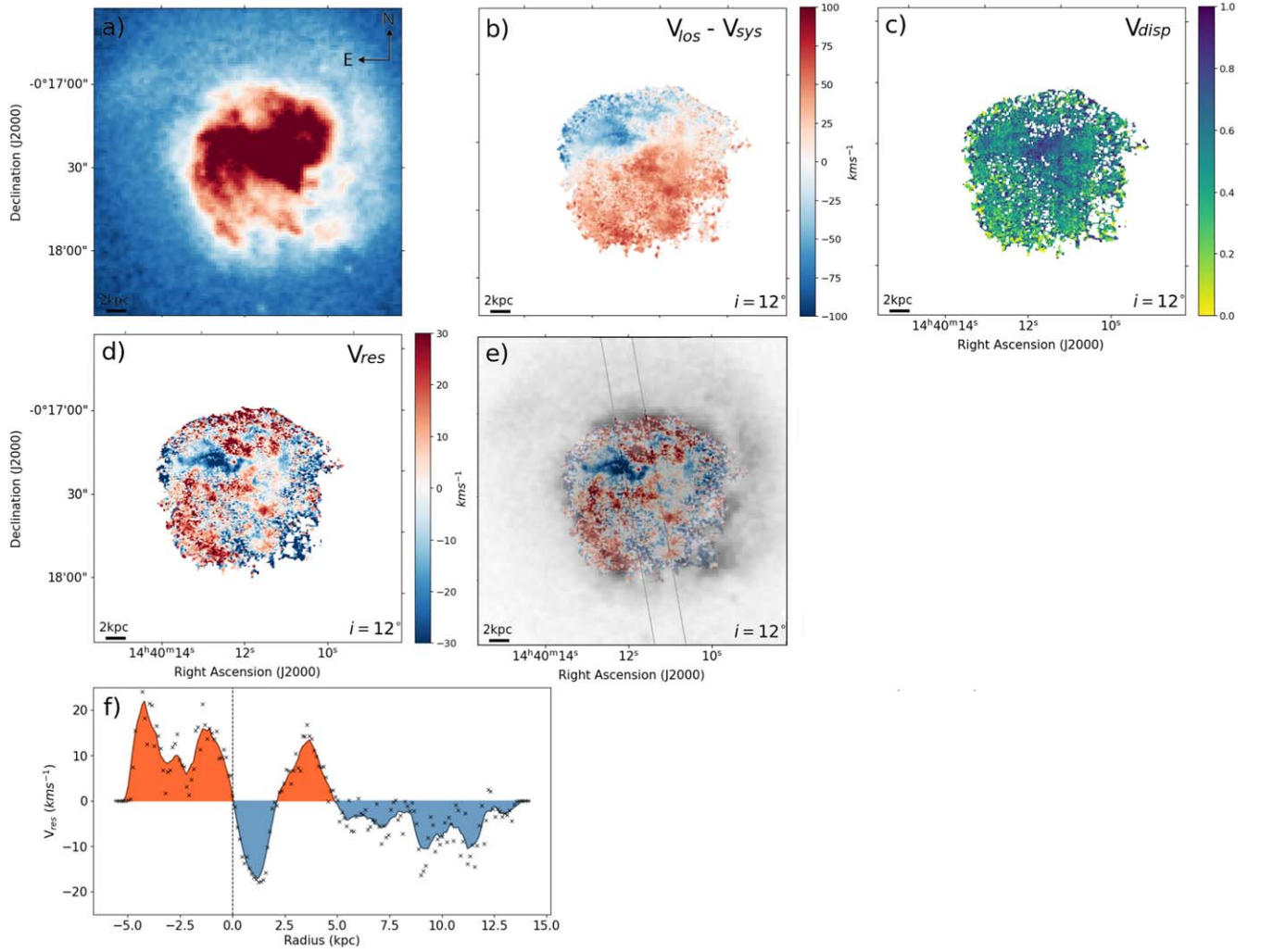


Figure 11. NGC 5713. Panel (a): XDFSS blue-band image. Panel (b): H_{α} velocity field. Panel (c): H_{α} velocity dispersion map normalized to 54.2 km s^{-1} corresponding to the 95th percentile. Panel (d): optical band image with the H_{α} residual velocity field. Panel (e): H_{α} residual velocity field. Panel (f): residual velocity radial profile considering a slit indicated by black lines with a PA of 170° in panel (e). The black line corresponds to the smoothed curve and the dashed line fits the center of the galaxy indicated in panel (e). The red (blue) area corresponds to velocities above (below) the midplane of the galaxy. The derived kinematic inclination is indicated in the lower right of each panel.

our pilot study based on VV304a (Gómez et al. 2021) brings this number to 22%. We note however that, as further discussed below, some of our observations were either not sufficient or not adequate to identify velocity perturbation on the disk outskirts, and thus, this percentage could be higher. In fact, out of the 40 galaxies in the WiNDS sample, only 70% show good H_{α} coverage. If we only consider this subset, the fraction of vertically perturbed galaxy candidates rises to 32%.

From the galaxies that show signs of potential vertical perturbation, six of them are interacting with a satellite galaxy and/or belong to a group. Thus, the observed kinematic perturbations are likely directly linked with recent environmental interactions. The rest of the perturbed subsample of galaxies are considered to be isolated. Therefore, their perturbations could be the result of previous minor mergers or misaligned cold gas accretion. A deeper and more detailed study must be performed for each galaxy to constrain the origin of their perturbed velocity field. As shown in Figure 1, the vertically perturbed candidates within the WiNDS sample (green distribution) show no preferential distribution of the main parameters with respect to the overall WiNDS sample.

Previous studies, either in HI (García-Ruiz et al. 2002) or in the optical (Reshetnikov & Combes 1998; Ann & Park 2006, for the edge-on galaxies) that have characterized the frequency that vertically perturbed disks arise in the local universe, have found that approximately 70% of them present a warped disk, typically displaying an S-shaped configuration. However, evidence for more complex corrugation patterns in external galaxies, such as those hinted at in this work, has been extremely scarce. Indeed, only a handful of previous studies have previously reported corrugations on external galaxies (e.g., Sánchez-Gil et al. 2015; Narayan et al. 2020; Gómez et al. 2021). In agreement with observations, cosmological simulations of high-resolution late-type galaxies within Milky Way-sized halos, Gómez et al. (2016, 2017) estimated that 70% should show strongly vertically perturbed disks, and 35% should present a corrugated structure. The scarcity in the detection of corrugation patterns on external galaxies so far was not that surprising since most studies attempting to characterize stellar disk vertical structures have been focused on edge-on systems in which corrugation is difficult to detect due to projection effects. Our study shows that high-resolution velocity maps, obtained with techniques such as an FP interferometer, allow

us to reveal much more complex velocity structures on external galactic disks. Furthermore, due to the low-inclination angles of the disks in our sample, these are likely linked with vertical flows and consistent with corrugation patterns. Eight galaxies from WiNDS show potential vertical patterns, of which 25% are in a close interaction with a massive companion, 50% show nearby dwarf satellite galaxies, and 25% can be regarded as isolated.

However, the fraction of low-inclination galaxies with detected velocity flow, i.e., $\approx 20\%$, is currently significantly lower than the expected fraction of vertically perturbed disks. Several factors could be playing a role here. The first and most obvious reason is that a fraction of $\approx 30\%$ of the galaxies in our sample did not show a wide H_α coverage. Such cases either presented a patchy and poor H_α emission distribution, or it was concentrated within the inner $\sim 0.5 R_{\text{opt}}$. As a result, we were not able to globally explore the kinematics of their disks, especially on the outer disk regions where warps and vertical perturbations are expected to be stronger. Second, the weather conditions in $\approx 12.5\%$ of our observations were not ideal. As a result, the observations were not sufficient to generate kinematic maps accurate enough to properly resolve their velocity fields. Considering these caveats, it is not surprising that we have been able to detect kinematic perturbation, consistent with a vertical perturbed disk, in a smaller fraction of galaxies than previously reported.

In a follow-up study, deeper and better observations will be presented. Following Gómez et al. (2021) we will compare our observations against detailed analytic kinematic models that account for the axisymmetric perturbations measured on each galaxy and thus constrain the origin of their velocity perturbations.

F.A.G. and C.U-M. acknowledge financial support from FONDECYT Regular 1211370. F.A.G., A.M., and C.U-M. gratefully acknowledge support by the ANID BASAL project FB210003 and funding from the Max Planck Society through a Partner Group grant. A.M. acknowledges financial support from FONDECYT Regular 1212046. F.M. acknowledges support through the Program “Rita Levi Montalcini” of the Italian MIUR. C.U-M also acknowledges financial support through the fellowship “Becas Doctorales Institucionales ULS”, granted by the Vicerrectoría de Investigación y Postgrado de la Universidad de La Serena. The WiNDS survey is based on observations taken at the Observatoire de Haute Provence (OHP, France), operated by the French CNRS. The authors warmly thank the OHP team for their technical assistance before and during the observations, namely, the night team: Jean Balcaen, Stéphane Favard, Jean-Pierre Troncin, Didier Gravallon, and the day team led by François Moreau as well as Dr. Auguste Le Van Suu. We are grateful to the whole SAM/SOAR team, who assisted us in the preparation and execution of the observations. This work was supported by the Programme National Cosmologie et Galaxies (PNCG) of CNRS/INSU with INP and IN2P3, cofunded by CEA and CNES. C.U-M. also acknowledges all the help and insights from Jesús Gómez-López and Gustavo Morales during the writing and data processing steps. The author also acknowledges Diego Pallero, Ciria Lima-Dias, and Daniel Hernández for their valuable discussions and comments.

Appendix A New Observation Data

A.1. Comments for Individual Galaxies

NGC 1058 is a nearly normal Sc face-on spiral galaxy with an inclination angle of 6° . NGC 1058 does not present well-

defined arms in H_α emission and reveals a weaker emission in the innermost than in the outer regions. The galaxy is located at a distance of 9.93 Mpc, the most recent work distance value is considered. It has an angular diameter of $3'$ with an apparent magnitude in the B band of about 12 mag. NGC 1058 belongs to the group NGC 1023 being the least bright member. This galaxy was observed in the H_α line (Sánchez-Gil et al. 2015) to analyze if it presents vertical flows using the long-slit technique using different PAs and finding that velocity peaks are associated with star-forming regions. Two supernovae 1961V and 1969L have been reported in the outer disk.

NGC 2500 is a nearby spiral galaxy with a short bar aligned with its minor kinematical axis, classified as SB(rs)d, located at 9.79 kpc at an inclination angle of 40° . This galaxy was observed using an H_α filter by Epinat et al. (2008a), who find diffuse emission in their observed H_α maps. NGC 2500's corrugated velocity patterns were studied using the long slits with H_α observations in Sánchez-Gil et al. (2015), where the vertical displacements do not seem to be related to an H_α emission peak. Like NGC 1058, this galaxy is part of the sample by Sánchez-Gil et al. (2015) but unlike in NGC 1058 where they find speed peaks, in NGC 2500 it was not conclusive.

NGC 3147 is a non-barred galaxy and it is classified as SA(rs)bc. It is considered the best type 2 Seyfert candidate using optical and X-ray observations, simultaneously (Bianchi et al. 2012).

NGC 3184 is a nearby grand-design spiral SABc type. Located at a distance of 10.05 Mpc, it has a nearly face-on orientation with inclination angles 16.7° and 184.5° deviated in this article using the methodology described previously. This galaxy belongs to the group NGC 3184 being the brightest with 9.7 mag. Other members are NGC 3198, NGC 3432, and NGC 3319.

NGC 3423 is a nearby spiral galaxy Sc type with an absolute B-band magnitude of 12 mag and angular size $3'.56$ and is located at 15 Mp. There are no previous analysis studies in particular of this galaxy.

NGC 3485 is a nearby spiral galaxy located at 28.17 Mpc with an absolute B-band magnitude of 12.7 mag. The kinematical inclination derived in this work is 26° . There are no individual works for this galaxy previously. In this work, the H_α emission is faint and is located in the galaxy arm.

NGC 3642 is a non-barred galaxy with three rings and dusty spiral arms classified as an SABc type. The galaxy shows a warped outer disk in the HI line (Verdes-Montenegro et al. 2002). NGC 3642 belongs to a group composed of five galaxies. NGC 3642 is the brightest member with elliptical galaxies NGC 3610 and NGC 3613 with similar magnitude. Another member is NGC 674, and NGC 3683 is fainter by more than 2 mag. It is an extended galaxy and shows around an internal disk from which a spiral arm appears that forms an external disk.

NGC 4136 is a nearby face-on galaxy with a bar and a ring as well as a well-developed spiral structure in its outer disk with low luminosity, and is classified as an SBc type (Gusev et al. 2003).

NGC 4900 is a spiral barred galaxy, classified as SB(rs)c located in the Virgo cluster at a distance of 13.3 Mpc and at about 12° southeast of M87. NGC 4900 presents an HII nucleus obtained with CO observations (Lee et al. 1998).

A.2. Presentation of the H_{α} Maps of the New Observation Data

The set of H_{α} maps of the new observations is available in the online journal.

A.3. Presentation of the H_{α} Monochromatic Maps of the Candidates of Vertically Perturbed Disks

The set of H_{α} monochromatic maps of the candidates of vertically perturbed disks is available in the online journal.

**Appendix B
Residual Maps of Additional Data Archive**

B.1. Residual Maps without Signs of Vertical Perturbations

The set of residual velocity maps without signs of vertical perturbations is available in the online journal.

**Appendix C
Rotation Curves of WiNDS**

C.1. Presentation of the Rotation Curves of WiNDS

The set of WiNDS rotation curves is available in the online journal.

**Appendix D
Image Processing**

D.1. Imaging Process for the Quantification of Vertical Perturbations on the V_{res} Field (Figure 12)

To highlight the larger velocity amplitudes in the V_{res} map, we use a filter on the residual field through Fourier transform and a Gaussian low-pass filter. The image filtering process is carried out following the process described in Figure 12.

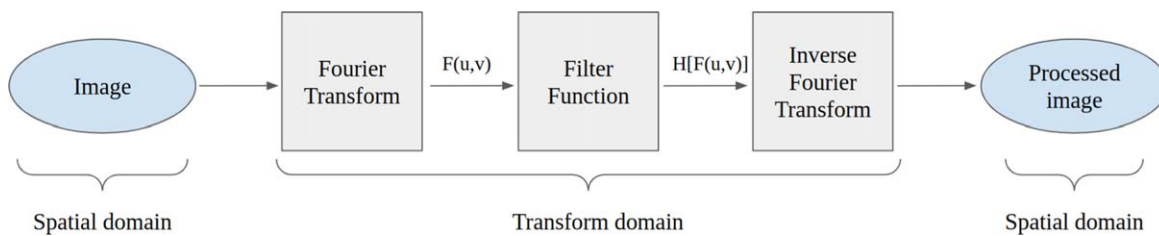


Figure 12. Sketch of the image processing pipeline adopted in this work.

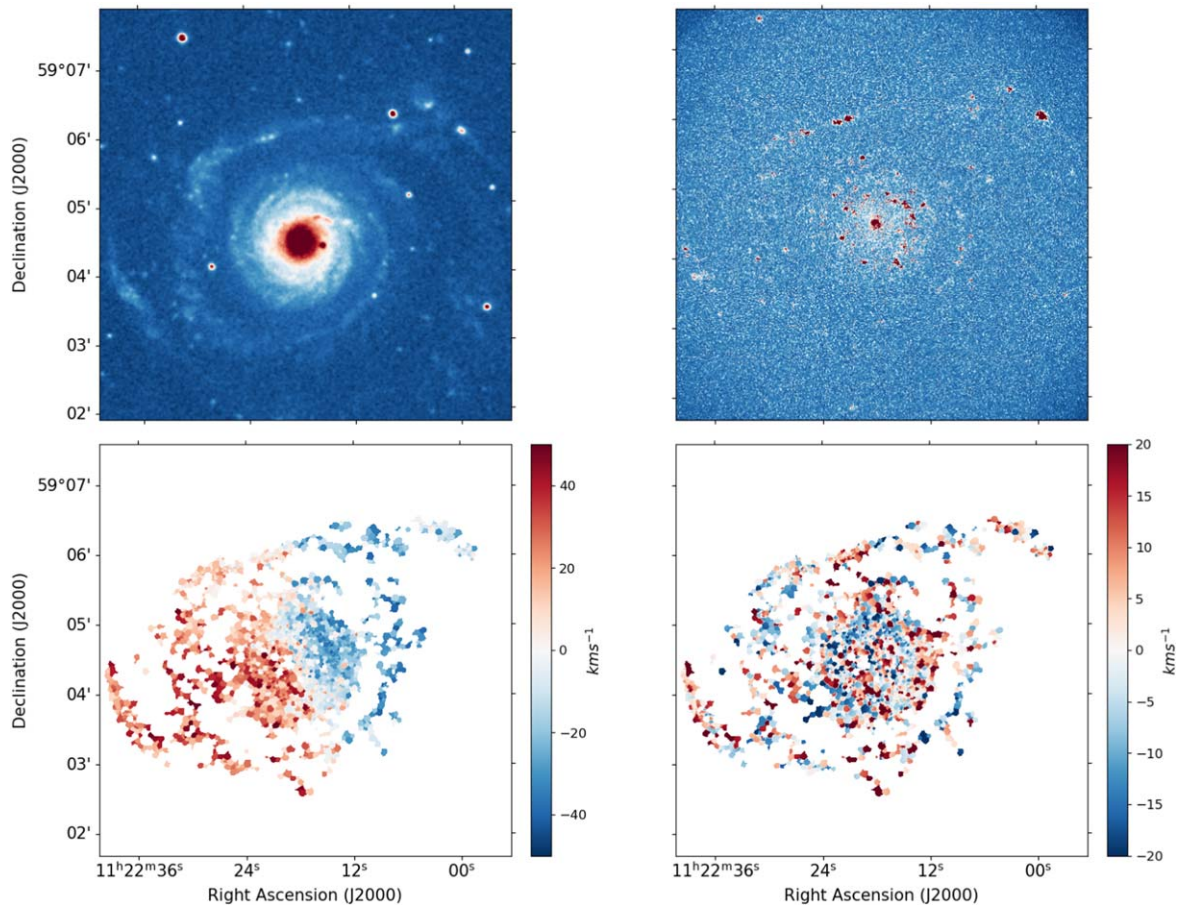


Figure 13. NGC 3642. Top left: X-DSS blue-band image. Top right: H_{α} monochromatic image. Bottom left: H_{α} velocity field. Bottom right: residual map H_{α} field. (The complete figure set (9 images) is available.)

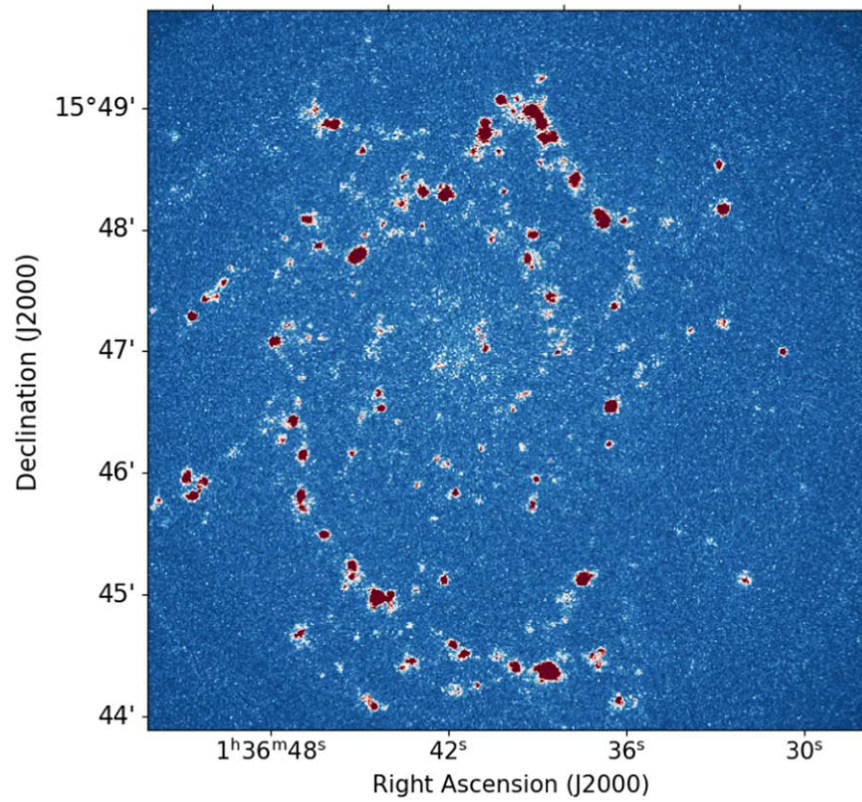


Figure 14. NGC 628. H α monochromatic image.
(The complete figure set (2 images) is available.)

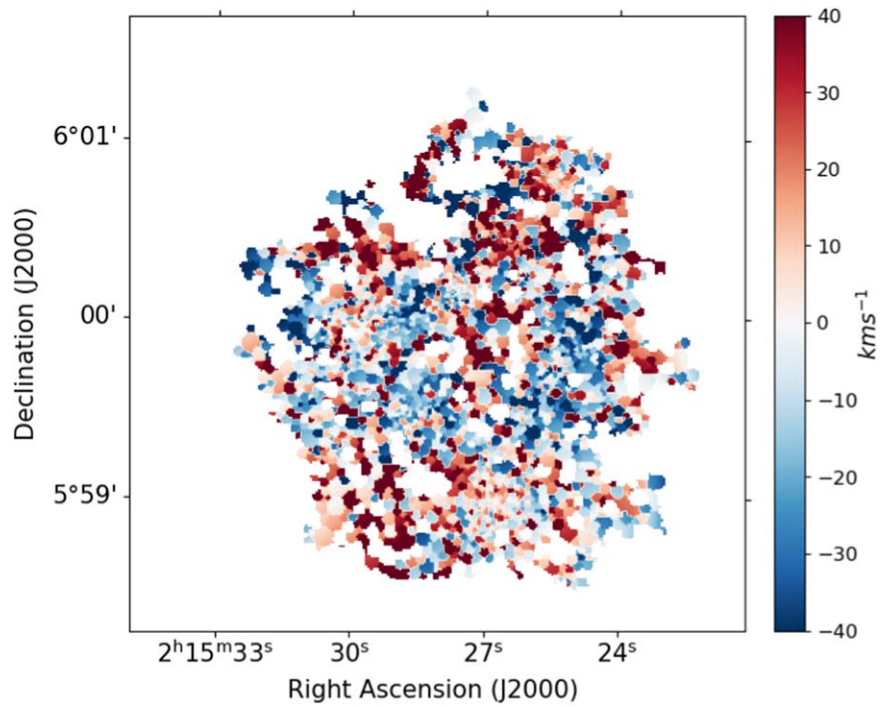


Figure 15. H α residual velocity of NGC 864.
(The complete figure set (4 images) is available.)

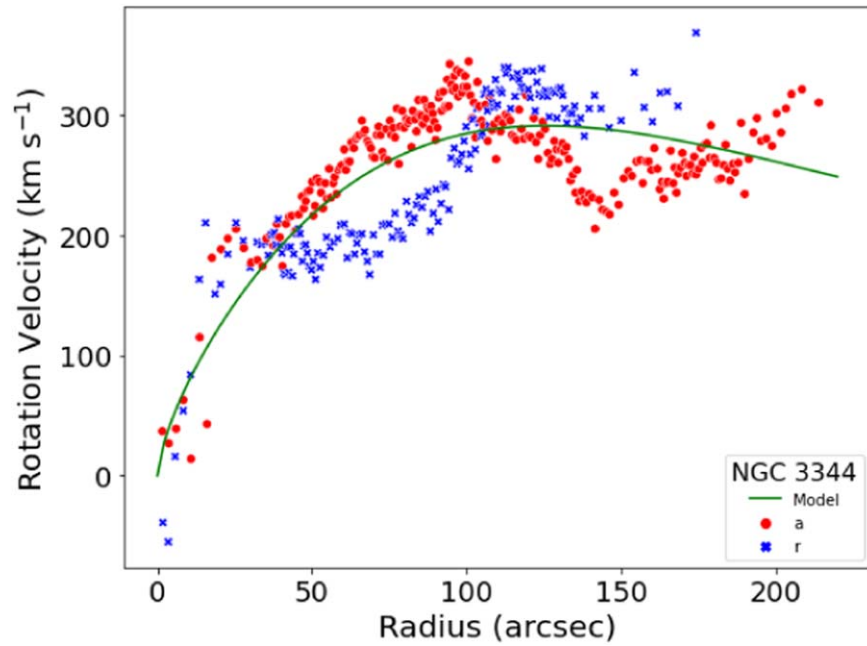


Figure 16. Rotation curves of NGC 3344.
(The complete figure set (6 images) is available.)

A spatial image $f(x, y)$ with dimension $N \times N$ in the Discrete Fourier Transform (DFT) of f called $F(u, v)$ is defined as

$$F(u, v) = \frac{1}{N} \sum_{x=0}^{N-1} \sum_{y=0}^{N-1} f(x, y) e^{-2\pi i(ux+vy)/N} \quad (\text{A1})$$

with $u = 0, 1, 2, \dots, N-1$, and $v = 0, 1, 2, \dots, N-1$, coordinates in Fourier space.

The inverse DFT is defined as

$$f(x, y) = \frac{1}{N} \sum_{u=0}^{N-1} \sum_{v=0}^{N-1} F(u, v) e^{2\pi i(ux+vy)/N}. \quad (\text{A2})$$



To remove or attenuate high frequencies in the Fourier domain, related to image noise, the Gaussian low-pass filter is used.

$$H(u, v) = e^{-D^2(u, v)/2D_0^2}, \quad (\text{A3})$$

where $D(u, v)$ corresponds to the Euclidean distance from (u, v) to the origin of the frequency plane and D_0 is the cutoff frequency in pixels in Fourier space.

ORCID iDs

Catalina Urrejola-Mora  <https://orcid.org/0000-0003-4747-4409>

Facundo A. Gómez  <https://orcid.org/0000-0002-1947-333X>
Antonela Monachesi  <https://orcid.org/0000-0003-2325-9616>

Federico Marinacci  <https://orcid.org/0000-0003-3816-7028>

References

Alfaro, E. J., Pérez, E., González Delgado, R. M., Martos, M. A., & Franco, J. 2001, *ApJ*, 550, 253
Amram, P., Mendes de Oliveira, C., Plana, H., Balkowski, C., & Hernandez, O. 2007, *A&A*, 471, 753
Ann, H. B., & Park, J. C. 2006, *NewA*, 11, 293

Antoja, T., Helmi, A., Romero-Gómez, M., et al. 2018, *Natur*, 561, 360
Aumer, M., White, S. D. M., Naab, T., & Scannapieco, C. 2013, *MNRAS*, 434, 3142
Bailin, J. 2003, *ApJL*, 583, L79
Begeman, K. G. 1987, PhD thesis, University of Groningen, Kapteyn Astronomical Institute
Begeman, K. G. 1989, *A&A*, 223, 47
Bianchi, S., Panessa, F., Barcons, X., et al. 2012, *MNRAS*, 426, 3225
Binggeli, B., Popescu, C. C., & Tammann, G. A. 1993, *A&AS*, 98, 275
Binggeli, B., Sandage, A., & Tammann, G. A. 1985, *AJ*, 90, 1681
Bland-Hawthorn, J., & Tepper-García, T. 2021, *MNRAS*, 504, 3168
Bland-Hawthorn, J., Sharma, S., Tepper-García, T., et al. 2019, *MNRAS*, 486, 1167
Boselli, A., Fossati, M., Gavazzi, G., et al. 2015, *A&A*, 579, A102
Briggs, F. H. 1986, *ApJ*, 300, 613
Briggs, F. H. 1990, *ApJ*, 352, 15
Chemin, L., Balkowski, C., Cayatte, V., et al. 2006, *MNRAS*, 366, 812
Daigle, O., Carignan, C., Amram, P., et al. 2006a, *MNRAS*, 367, 469
Daigle, O., Carignan, C., Hernandez, O., Chemin, L., & Amram, P. 2006b, *MNRAS*, 368, 1016
de Vaucouleurs, G., de Vaucouleurs, A., Corwin, H. G., et al. 1991, Third Reference Catalogue of Bright Galaxies (New York: Springer)
Debatista, V. P., & Sellwood, J. A. 1999, *ApJL*, 513, L107
DeBuhr, J., Ma, C.-P., & White, S. D. M. 2012, *MNRAS*, 426, 983
Dicaire, I., Carignan, C., Amram, P., et al. 2008, *MNRAS*, 385, 553
D’Onghia, E., Madau, P., Vera-Ciro, C., Quillen, A., & Hernquist, L. 2016, *ApJ*, 823, 4
Epinat, B., Amram, P., & Marcelin, M. 2008a, *MNRAS*, 390, 466
Epinat, B., Amram, P., Marcelin, M., et al. 2008b, *MNRAS*, 388, 500
Gaia Collaboration, Antoja, T., McMillan, P., et al. 2021, *A&A*, 649, A8
Gaia Collaboration, Katz, D., Antoja, T., et al. 2018, *A&A*, 616, A11
García-Ruiz, I., Sancisi, R., & Kuijken, K. 2002, *A&A*, 394, 769
Gómez, F. A., Minchev, I., O’Shea, B. W., et al. 2013, *MNRAS*, 429, 159
Gómez, F. A., White, S. D. M., Grand, R. J. J., et al. 2017, *MNRAS*, 465, 3446
Gómez, F. A., White, S. D. M., Marinacci, F., et al. 2016, *MNRAS*, 456, 2779
Gómez, F. A., Torres-Flores, S., Mora-Urrejola, C., et al. 2021, *ApJ*, 908, 27
Gómez-López, J. A., Amram, P., Epinat, B., et al. 2019, *A&A*, 631, A71
Gooch, R. 1996, in ASP Conf. Ser. 101, Astronomical Data Analysis Software and Systems V (San Francisco, CA: ASP), 80
Grand, R. J. J., Gómez, F. A., Marinacci, F., et al. 2017, *MNRAS*, 467, 179
Gusev, A. S., Zasov, A. V., & Kaisin, S. S. 2003, *AstL*, 29, 363
Haan, S., & Braun, R. 2014, *MNRAS*, 443, 186
Haynes, M. P., Giovanelli, R., Kent, B. R., et al. 2018, *ApJ*, 861, 49
Hernandez, O., Wozniak, H., Carignan, C., et al. 2005, *ApJ*, 632, 253

- James, P. A., Shane, N. S., Beckman, J. E., et al. 2004, *A&A*, 414, 23
- Jiang, I.-G., & Binney, J. 1999, *MNRAS*, 303, L7
- Jiménez-Vicente, J., & Battaner, E. 2000, *A&A*, 358, 812
- Kamphuis, J., & Briggs, F. 1992, *A&A*, 253, 335
- Karachentsev, I. D., Kajsín, S. S., Tsvetanov, Z., & Ford, H. 2005, *A&A*, 434, 935
- Karachentsev, I. D., Makarov, D. I., & Kaisina, E. I. 2013, *AJ*, 145, 101
- Karachentsev, I. D., Sharina, M. E., & Huchtmeier, W. K. 2000, *A&A*, 362, 544
- Kazantzidis, S., Zentner, A. R., Kravtsov, A. V., Bullock, J. S., & Debattista, V. P. 2009, *ApJ*, 700, 1896
- Kennicutt, R. C. J., Armus, L., Bendo, G., et al. 2003, *PASP*, 115, 928
- Knapen, J. H., Cepa, J., Beckman, J. E., Soledad del Río, M., & Pedlar, A. 1993, *ApJ*, 416, 563
- Laporte, C. F. P., Agnello, A., & Navarro, J. F. 2019, *MNRAS*, 484, 245
- Laporte, C. F. P., Belokurov, V., Koposov, S. E., Smith, M. C., & Hill, V. 2020, *MNRAS*, 492, L61
- Laporte, C. F. P., Gómez, F. A., Besla, G., Johnston, K. V., & Garavito-Camargo, N. 2018a, *MNRAS*, 473, 1218
- Laporte, C. F. P., Johnston, K. V., Gómez, F. A., Garavito-Camargo, N., & Besla, G. 2018b, *MNRAS*, 481, 286
- Lee, H. M., Kim, H., & Ann, H. 1998, *JKAS*, 31, 95
- López-Corredoira, M., Cabrera-Lavers, A., Garzón, F., & Hammersley, P. L. 2002, *A&A*, 394, 883
- Mendes de Oliveira, C., Amram, P., Quint, B. C., et al. 2017, *MNRAS*, 469, 3424
- Michałowski, M. J., Gotkiewicz, N., Hjorth, J., & Kamphuis, P. 2020, *A&A*, 638, A47
- Momany, Y., Zaggia, S., Gilmore, G., et al. 2006, *A&A*, 451, 515
- Monari, G., Famaey, B., Siebert, A., et al. 2016, *MNRAS*, 461, 3835
- Narayan, C. A., Dettmar, R.-J., & Saha, K. 2020, *MNRAS*, 495, 3705
- Oikawa, S., & Sofue, Y. 2014, *PASJ*, 66, 77
- Ostriker, E. C., & Binney, J. J. 1989, *MNRAS*, 237, 785
- Paturel, G., Andernach, H., Bottinelli, L., et al. 1997, *A&AS*, 124, 109
- Pisano, D. J., & Wilcots, E. M. 2000, *MNRAS*, 319, 821
- Press, W. H., Teukolsky, S. A., Vetterling, W. T., & Flannery, B. P. 1992, *Numerical Recipes in C: The Art of Scientific Computing* (Cambridge: Cambridge Univ. Press)
- Price-Whelan, A. M., Johnston, K. V., Sheffield, A. A., Laporte, C. F. P., & Sesar, B. 2015, *MNRAS*, 452, 676
- Quinn, P. J., Hernquist, L., & Fullagar, D. P. 1993, *ApJ*, 403, 74
- Radburn-Smith, D. J., de Jong, R. S., Streich, D., et al. 2014, *ApJ*, 780, 105
- Reshetnikov, V., & Combes, F. 1998, *A&A*, 337, 9
- Rots, A. H., Bosma, A., van der Hulst, J. M., Athanassoula, E., & Crane, P. C. 1990, *AJ*, 100, 387
- Roškar, R., Debattista, V. P., Brooks, A. M., et al. 2010, *MNRAS*, 408, 783
- Sánchez-Gil, M. C., Alfaro, E. J., & Pérez, E. 2015, *MNRAS*, 454, 3376
- Sancisi, R., Fraternali, F., Oosterloo, T., & van der Hulst, T. 2008, *A&ARv*, 15, 189
- Schinnerer, E., Böker, T., Emsellem, E., & Lisenfeld, U. 2006, *ApJ*, 649, 181
- Schulman, E., Bregman, J. N., Brinks, E., & Roberts, M. S. 1996, *AJ*, 112, 960
- Sellwood, J. A. 2013, in *Dynamics of Disks and Warps*, ed. T. D. Oswalt & G. Gilmore, Vol. 5 (Dordrecht: Springer Science+Business Media), 923
- Shen, J., & Sellwood, J. A. 2006, *MNRAS*, 370, 2
- Sheth, K., Regan, M., Hinz, J. L., et al. 2010, *PASP*, 122, 1397
- Shetty, R., Vogel, S. N., Ostriker, E. C., & Teuben, P. J. 2007, *ApJ*, 665, 1138
- Slater, C. T., Bell, E. F., Schlafly, E. F., et al. 2014, *ApJ*, 791, 9
- Tully, R. B. 1988, *Nearby Galaxies Catalog* (Cambridge: Cambridge Univ. Press)
- van der Hulst, J. M., van Albada, T. S., & Sancisi, R. 2001, in *ASP Conf. Ser. 240, Gas and Galaxy Evolution*, ed. J. E. Hibbard, M. Rupen, & J. H. van Gorkom (San Francisco, CA: ASP), 451
- Velazquez, H., & White, S. D. M. 1999, *MNRAS*, 304, 254
- Verdes-Montenegro, L., Bosma, A., & Athanassoula, E. 2000, *A&A*, 356, 827
- Verdes-Montenegro, L., Bosma, A., & Athanassoula, E. 2002, *A&A*, 389, 825
- Vergani, D., Pizzella, A., Corsini, E. M., et al. 2007, *A&A*, 463, 883
- Vesperini, E., & Weinberg, M. D. 2000, *ApJ*, 534, 598
- Walter, F., Brinks, E., de Blok, W. J. G., et al. 2008, *AJ*, 136, 2563
- Warner, P. J., Wright, M. C. H., & Baldwin, J. E. 1973, *MNRAS*, 163, 163
- Weinberg, M. D. 1998, *MNRAS*, 299, 499
- Widrow, L. M., Barber, J., Chequers, M. H., & Cheng, E. 2014, *MNRAS*, 440, 1971
- Widrow, L. M., Gardner, S., Yanny, B., Dodelson, S., & Chen, H.-Y. 2012, *ApJL*, 750, L41
- Xu, Y., Newberg, H. J., Carlin, J. L., et al. 2015, *ApJ*, 801, 105
- York, D. G., Adelman, J., Anderson, J. E., Jr., et al. 2000, *AJ*, 120, 1579
- Yurin, D., & Springel, V. 2015, *MNRAS*, 452, 2367